Journal of Computational Physics (2024)

Contents lists available at ScienceDirect

Journal of Computational Physics

journal homepage: www.elsevier.com/locate/jcp

Simplified conservative discretization of the Cahn-Hilliard-Navier-Stokes equations

Jason Goulding[a], Mehrnaz Ayazi[a], Tamar Shinar[a,*], Craig Schroeder[a,*]

[a]*Department of Computer Science and Engineering, University of California, Riverside, 351 Winston Chung Hall, Riverside, CA 92521-0429, USA*

ARTICLE INFO

Article history:

ABSTRACT

In this paper we construct a novel discretization of the Cahn-Hilliard equation coupled with the Navier-Stokes equations. The Cahn-Hilliard equation models the separation of a binary mixture. We construct a very simple time integration scheme for simulating the Cahn-Hilliard equation, which is based on splitting the fourth-order equation into two second-order Helmholtz equations. We combine the Cahn-Hilliard equation with the Navier-Stokes equations to simulate phase separation in a two-phase fluid flow in two dimensions. The scheme conserves mass and momentum and exhibits consistency between mass and momentum, allowing it to be used with large density ratios. We introduce a novel discretization of the surface tension force from the phase-field variable that has finite support around the transition region. The model has a parameter that allows it to transition from a smoothed continuum surface force to a fully sharp interface formulation. We show that our method achieves second-order accuracy, and we compare our method to previous work in a variety of experiments.

1. Introduction

Phase-field models have been widely used to study many problems involving multiphase incompressible flows, including two-phase flows in a microtube [27], viscoelastic flows [61, 62], multiphase flows with soluble surfactants [45, 54, 63], phase separation and coarsening [64, 2], jet pinch-off [60, 38], multicomponent systems with three or more phases [39, 36, 59], tumor growth [58], microfluidics [50], and other physical phenomena. In these methods, the phase field represents the concentration of one of the components of the mixture, and fluid interfaces are represented by a smooth transition region between bulk regions of the different phases. One popular choice for the governing equation for the evolution of the phase field is the Cahn-Hilliard equation, which acts to minimize the free energy of the system, leading the mixture to segregate into separate regions [8, 15].

*Corresponding authors: email: shinar@cs.ucr.edu, craigs@cs.ucr.edu

Many methods have been developed for the numerical simulation of the Cahn-Hilliard equation, including Fourier spectral methods [64, 28, 41], finite difference methods [19, 42, 23, 9, 31], and finite element methods [16, 5, 4, 17, 57, 26]. For example, Zhu et al. [64] examines properties of coarsening using a Fourier spectral solver, and He et al. [28] developed a Fourier spectral solve which allows for large time steps. Schemes supporting adaptive time step sizes were presented in Li et al. [43] and the second-order accurate Guillén-González and Tierra [22]. Guillén-González and Tierra [21] presented two linear schemes derived through special treatment of the double-well potential function. Lee et al. [41] gives an overview of the mathematical derivation of the Cahn-Hilliard equation, discusses several methods for its numerical solution, and provides a Matlab implementation for a pseudospectral method.

A model of immiscible two-phase flows coupling the Cahn-Hilliard equation to the incompressible Navier-Stokes equations for the case of matching densities was described in Hohenberg and Halperin [29]; a derivation from first principles was given in Gurtin et al. [24]. Badalassi et al. [3] devised numerical simulations of this coupled system. For varying densities, some studies have used the Boussinesq approximation where the momentum equation is solved using a background density and the variable density appears only in additional buoyancy terms [32, 44, 2]. The more general case of the Cahn-Hilliard-Navier-Stokes (CHNS) equations with different densities and viscosities presents additional challenges, and Shen and Yang [52] devised a model which admits an energy law and developed an associated projection-type [10] numerical scheme. Shen and Yang [51] developed an unconditionally energy-stable numerical scheme which reduces the problem to the solution of a sequence of decoupled elliptic solves. Phase-field models of two-phase incompressible flow with large density ratios were simulated in Kim [35] and Ding et al. [12], which involved the solution of time-dependent variable coefficient linear systems. Dong and Shen [14] devised a scheme for large density and viscosity differences with improved efficiency through the use of constant coefficient matrices. Yue et al. [61] coupled the Cahn-Hilliard equation to non-Newtonian flows. Guo et al. [23] devised a quasi-incompressible scheme with mass conservative and energy stability for the CHNS equations. Kim [38] provides a review of phase-field models and numerical methods for their approximation.

Consistency of mass and momentum transport was first addressed on the discrete level for two-phase interfacial flows in volume-tracking methods [7, 47] and the level set method [48]. For the coupled Cahn-Hilliard-Navier-Stokes equations, Huang et al. [31] formulated a set of consistency conditions in the continuous setting and furthermore devised a second-order accurate finite difference scheme with numerical consistency of mass and momentum flux. Huang et al. [30] similarly addressed consistency of mass and momentum transport in the Allen-Cahn equation and also devised a conservative redistribution scheme to maintain the physical bounds of the concentration.

In this work, we construct a novel conservative, second order accurate finite difference scheme for the simulation of the Cahn-Hilliard-Navier-Stokes equations for two phase flows with large density and viscosity differences. Following Huang et al. [31], we enforce discrete consistency of the mass and momentum fluxes. In contrast to Huang et al. [31], which used collocated grids for pressure, concentration, and velocity, our method uses a staggered MAC grid [25] to conveniently solve the pressure Poisson equation. We construct a very simple time integration scheme for simulating the Cahn-Hilliard equation, which is based on splitting the fourth-order equation into two second-order Helmholtz equations. Our splitting results in the solution of two Helmholtz equations with identical coefficient matrices. In our splitting, we use a stabilizing term introduced in Shen and Yang [51, 52].

The Cahn-Hilliard equation is coupled to the Navier-Stokes equations in part through the surface tension force, which depends on the gradient of the concentration phase field and the geometric curvature of the interface. Kim [35, 38] and Acar [1] discuss several models of surface tension for phase-field multiphase flows. The numerical simulation of surface tension can be challenging due to stability and accuracy issues including the formation of spurious currents about the interface. One common treatment of surface tension is the Continuum Surface Force (CSF) approach introduced in Brackbill et al. [6], where typically a discrete approximation to a smoothed delta function is used to spread the surface tension force over a small number of grid cells about the interface. Kim [37] used a continuum surface force combinations for more than two fluid phases. Another set of approaches treats the interface in a sharp manner, capturing the pressure jumps across the interface that balance the surface tension force [34]. Francois et al. [18] enforced exact force balance at the interface for both CSF and sharp interface schemes, eliminating one of the sources of spurious currents at the interface. In this work, we propose a novel discretization of surface tension that gives exact force balance at the interface and unifies the CSF and sharp interfaces schemes. A similar relationship between the CSF approach and the sharp interface approach was noted by Lalanne et al. [40] for level set methods. Our method is based on taking the gradient of a smoothed Heaviside approximation, similar to CSF approaches. Notably, the degree of smoothing is controlled by a parameter and the sharp interface method is directly recovered as the smoothing is decreased.

2. Governing equations

2.1. Cahn-Hilliard Equation

The Cahn-Hilliard equation, initially proposed by Cahn and Hilliard [8] and widely utilized to describe the phase separation process in a mixture of two fluids, is expressed as follows:

$$\frac{\partial \gamma}{\partial t} + \nabla \cdot (\mathbf{u}\gamma) = \nabla \cdot (M \nabla \xi) + S_\gamma \tag{1}$$

$$\xi = \lambda(F'(\gamma) - \nabla^2 \gamma) \tag{2}$$

$$F(\gamma) = \frac{1}{\eta^2}\gamma^2(1-\gamma)^2 \tag{3}$$

$$\lambda = \frac{3}{2\sqrt{2}}\sigma\eta. \tag{4}$$

The phase-field function $\gamma \in [0, 1]$ is the volume fraction of fluid phase 1 (with density ρ_1 and viscosity μ_1). $1 - \gamma$ is the volume fraction of fluid phase 0 (with density ρ_0 and viscosity μ_0). $\mathbf{u}$ is the velocity, M is the mobility, ξ is the chemical potential, S_γ is the source term for γ, λ is the mixing energy density, F is the double well potential function, F' is the derivative of F with respect to γ, η characterizes the thickness of the transition region between the two phases, and σ is the surface tension coefficient. The effective density and viscosity at a certain location is given by

$$\rho = \rho_0 + (\rho_1 - \rho_0)\,\gamma \tag{5}$$

$$\mu = \mu_0 + (\mu_1 - \mu_0)\,\gamma. \tag{6}$$

2.2. Navier-Stokes equations

The incompressible Navier-Stokes equations are given by

$$\frac{\partial \rho}{\partial t} + \nabla \cdot \mathbf{m} = S_m \tag{7}$$

$$\nabla \cdot \mathbf{u} = 0 \tag{8}$$

$$\frac{\partial(\rho\mathbf{u})}{\partial t} + \nabla \cdot (\mathbf{m} \otimes \mathbf{u}) = -\nabla p + \nabla \cdot (\mu(\nabla \mathbf{u} + (\nabla \mathbf{u})^T)) + \rho g + \sigma\kappa\nabla(g(\gamma)) + S_{\mathbf{u}}. \tag{9}$$

σ, ρ, and $\mathbf{u}$ are as defined in Section 2.1, $\mathbf{m}$ is the mass flux, S_m represents an external source of mass, $\sigma\kappa\nabla g(\gamma)$ is the surface tension force, κ is the estimated interface curvature, $g(\gamma)$ is a regularized Heaviside function (see Section 3.2.3), p is the pressure, $\mathbf{g}$ is gravity, and S_u is the source term for momentum. Similar to [31], the mass flux $\mathbf{m}$ can be inferred from the γ evolution equation (1) and equations (7) and (5). Defining $S_m = (\rho_1 - \rho_0)\,S_\gamma$, it can be shown that a consistent definition of $\mathbf{m}$ is $\mathbf{m} = \rho\mathbf{u} - (\rho_1 - \rho_0)\,M\nabla\xi$. This is discussed in detail in Section 3.2.2.

3. Discretizations

In this section we describe the temporal and spatial discretizations of the Cahn-Hilliard and Navier-Stokes equations.

3.1. Cahn-Hilliard equation

Although the overall form for the splitting of the CH equations follows the same general strategy as prior discretizations, we achieve a discretization that is significantly simpler than existing discretizations while not sacrificing desirable features of the discretization. Our discretization of the Navier-Stokes equations was designed to be as similar to a standard second-order MAC-grid discretization as possible while still achieving favorable numerical properties when coupling with the Cahn-Hilliard equations.

3.1.1. Cahn-Hilliard equation temporal discretization

We begin by combining (1) and (2) as the base Cahn-Hilliard equation to discretize.

$$\frac{\partial \gamma}{\partial t} + \nabla \cdot (\mathbf{u}\gamma) = M\lambda\nabla^2(F'(\gamma) - \nabla^2\gamma) + S_\gamma \tag{10}$$

We discretize the time derivative as $\frac{\alpha\hat{\gamma}^{n+1} - \alpha\gamma^{BD}}{\Delta t}$. To achieve second-order accuracy, we use a backwards-difference scheme with $\alpha = \frac{3}{2}$ and $\gamma^{BD} = \frac{4}{3}\gamma^n - \frac{1}{3}\gamma^{n-1}$. For the first time step we use a first-order single-step scheme with $\alpha = 1$ and $\gamma^{BD} = \gamma^n$. Explicit quantities for $\mathbf{u}$ and γ are discretized using an Adams-Bashforth scheme, where $\gamma^{AB} = \gamma^n$, $\mathbf{u}^{AB} = \mathbf{u}^n$ in the first order case and $\gamma^{AB} = 2\gamma^n - \gamma^{n-1}$, $\mathbf{u}^{AB} = 2\mathbf{u}^n - \mathbf{u}^{n-1}$ in the second order case. Since in practice α and Δt always occur together, we let $\Delta t = \alpha\widehat{\Delta t}$. $\hat{\gamma}^{n+1}$ represents an estimate of the final γ obtained by solving this discretized equation; it will be later updated to the final γ^{n+1} bounded to the range $[0, 1]$ using the method described in Section 3.1.2.

Following Shen and Yang [52], we introduce a term $2\tau\left(\hat{\gamma}^{n+1} - \gamma^{AB}\right)$ to help with splitting the equation. The choice of τ is discussed below. Since both $\hat{\gamma}^{n+1}$ and γ^{AB} are estimates of γ^{n+1}, this term vanishes rapidly under refinement.

$$\frac{\hat{\gamma}^{n+1} - \gamma^{BD}}{\widehat{\Delta t}} + \nabla \cdot \left(\mathbf{u}^{AB}\gamma^{AB}\right) = M\lambda\nabla^2\left(F'\left(\gamma^{AB}\right) - \nabla^2\hat{\gamma}^{n+1} + 2\tau\left(\hat{\gamma}^{n+1} - \gamma^{AB}\right)\right) + S_\gamma^{n+1} \tag{11}$$

Next we split out the advection term as an update from γ^{BD} to γ^*:

$$\frac{\gamma^* - \gamma^{BD}}{\widehat{\Delta t}} + \nabla \cdot \left(\mathbf{u}^{AB}\gamma^{AB}\right) = 0 \tag{12}$$

$$\frac{\hat{\gamma}^{n+1} - \gamma^*}{\widehat{\Delta t}} = M\lambda\nabla^2\left(F'\left(\gamma^{AB}\right) - \nabla^2\hat{\gamma}^{n+1} + 2\tau\left(\hat{\gamma}^{n+1} - \gamma^{AB}\right)\right) + S_\gamma^{n+1}. \tag{13}$$

We group all explicit terms under the Laplacian into a new term A:

$$A = \frac{1}{\tau}F'\left(\gamma^{AB}\right) - 2\gamma^{AB} \tag{14}$$

$$\frac{\hat{\gamma}^{n+1} - \gamma^*}{\widehat{\Delta t}} = M\lambda\nabla^2\left(\tau A - \nabla^2\hat{\gamma}^{n+1} + 2\tau\hat{\gamma}^{n+1}\right) + S_\gamma^{n+1} \tag{15}$$

Grouping together $\hat{\gamma}^{n+1}$ with $\nabla^2\hat{\gamma}^{n+1}$ on both sides of the equation:

$$\frac{\left(\hat{\gamma}^{n+1} - \tau M\lambda\widehat{\Delta t}\nabla^2\hat{\gamma}^{n+1} + A\right) - \gamma^*}{\widehat{\Delta t}} = \tau M\lambda\nabla^2\left(\hat{\gamma}^{n+1} - \frac{1}{\tau}\nabla^2\hat{\gamma}^{n+1} + A\right) + \frac{A}{\widehat{\Delta t}} + S_\gamma^{n+1}. \tag{16}$$

For the two parenthesized expressions to match, we need $\tau^2 M\lambda\widehat{\Delta t} = 1$. We achieve this by letting

$$s = \sqrt{\frac{M\lambda}{\widehat{\Delta t}}} \qquad \tau = \frac{1}{M\lambda}s \tag{17}$$

and define

$$\gamma' = \hat{\gamma}^{n+1} - s\widehat{\Delta t}\nabla^2\hat{\gamma}^{n+1} + A. \tag{18}$$

With these definitions, equation (16) becomes

$$\frac{\gamma' - \gamma^*}{\widehat{\Delta t}} = s\nabla^2\gamma' + \frac{1}{\widehat{\Delta t}}A + S_\gamma^{n+1}. \tag{19}$$

Observe that (18) and (19) are implicit Helmholtz equations for $\hat{\gamma}^{n+1}$ and γ', respectively. Note that while differing from the stabilizing term introduced in Shen and Yang [52], our choice of τ results in a conditionally stable scheme, as shown in Section 4.1. With our choice of τ, the overall term is formally 1.5 order accurate (although within the resolutions studied below, our method exhibits second-order convergence). While the first-order stabilizing scheme in Shen and Yang [52] uses the difference $\gamma^{n+1} - \gamma^n$, we also note that [52] additionally introduced a second-order stabilizing term based on $\gamma^{n+1} - \gamma^{AB}$ as part of a second order scheme.

3.1.2. Cahn-Hilliard bounds-respecting redistribution scheme

When solving the Cahn-Hilliard equation, numerical errors or sufficiently large time steps can result in γ outside the range $[0, 1]$. Given a large density ratio between the fluids, this can result in negative densities from (5). In order to prevent this, we use a redistribution scheme for γ as detailed in Huang et al. [30] adapted for the range $[0, 1]$.

First $\hat{\gamma}^{n+1}$ is clamped to the feasible range at each index i, j:

$$\gamma_{i,j}^{b*} = \begin{cases} 1, & \text{if } \hat{\gamma}_{i,j}^{n+1} \geq 1 \\ 0, & \text{if } \hat{\gamma}_{i,j}^{n+1} \leq 0 \\ \hat{\gamma}_{i,j}^{n+1}, & \text{otherwise.} \end{cases} \tag{20}$$

The total difference between γ^{b*} and $\hat{\gamma}^{n+1}$ is then redistributed among all indices using a weight function:

$$W_b(\gamma) = 4\gamma - 4\gamma^2 \tag{21}$$

$$\gamma_{i,j}^{n+1} = \gamma_{i,j}^{b*} + \frac{W_b\left(\gamma_{i,j}^{b*}\right)}{\sum_{r,s} W_b\left(\gamma_{r,s}^{b*}\right)} \sum_{r,s} \left(\hat{\gamma}_{r,s}^{n+1} - \gamma_{r,s}^{b*}\right). \tag{22}$$

The indices r, s are over the entire computational domain, and a uniform grid is assumed. Since this update is globally conservative, we can express the change in the final quantity γ^{n+1} as the divergence of an unknown weighted gradient term $W_b\left(\gamma^{n+1}\right)\nabla Q$ with no-flux boundary conditions. This results in a Poisson equation for Q:

$$\frac{\gamma^{n+1} - \hat{\gamma}^{n+1}}{\widehat{\Delta t}} = \nabla \cdot \left(W_b\left(\gamma^{n+1}\right)\nabla Q\right), \tag{23}$$

$$\mathbf{n} \cdot \nabla Q = 0 \tag{24}$$

which we solve and use to compute the density flux $\mathbf{m}$ (See Section 3.2.2).

3.1.3. Cahn-Hilliard boundary conditions

In this paper, we consider two types of boundary conditions for γ: periodic and Neumann ($\mathbf{n} \cdot \nabla\hat{\gamma}^{n+1} = 0$). Since the Cahn-Hilliard equation is fourth order, we require another boundary condition; Noting (13)

$$\frac{\hat{\gamma}^{n+1} - \gamma^*}{\widehat{\Delta t}} = M\lambda\nabla^2\left(F'(\gamma^{AB}) - \nabla^2\hat{\gamma}^{n+1} + \frac{2s}{M\lambda}\left(\hat{\gamma}^{n+1} - \gamma^{AB}\right)\right) + S_\gamma^{n+1} \tag{25}$$

we define ξ^* to be a discrete version of the chemical potential from (2) as

$$\xi^* = \lambda\left(F'\left(\gamma^{AB}\right) - \nabla^2\hat{\gamma}^{n+1} + \frac{2s}{M\lambda}\left(\hat{\gamma}^{n+1} - \gamma^{AB}\right)\right) \tag{26}$$

$$= \lambda\left(\tau A - \nabla^2\hat{\gamma}^{n+1} + 2\tau\hat{\gamma}^{n+1}\right) \tag{27}$$

$$= \tau\lambda\left(\hat{\gamma}^{n+1} - \frac{1}{\tau}\nabla^2\hat{\gamma}^{n+1} + A + \hat{\gamma}^{n+1}\right) \tag{28}$$

$$= \frac{s}{M}\left(\gamma' + \hat{\gamma}^{n+1}\right). \tag{29}$$

Following [31] we use the boundary condition $\mathbf{n} \cdot \nabla\xi^* = 0$, which leads to $\mathbf{n} \cdot \nabla\gamma' = 0$. This gives us the necessary boundary conditions for both of our Helmholtz systems.

3.2. Navier-Stokes equations

3.2.1. Navier-Stokes temporal discretization

As in Section 3.1.1, we discretize the time derivative as $\frac{\alpha\rho^{n+1}\mathbf{u}^{n+1} - \alpha(\rho\mathbf{u})^{BD}}{\Delta t}$. For the first time step, $\alpha = 1$ and $(\rho\mathbf{u})^{BD} = \rho^n\mathbf{u}^n$. To achieve second-order accuracy, we thereafter use a backwards-difference scheme with $\alpha = \frac{3}{2}$ and $(\rho\mathbf{u})^{BD} = \frac{4}{3}\rho^n\mathbf{u}^n - \frac{1}{3}\rho^{n-1}\mathbf{u}^{n-1}$. Explicit quantities for $\mathbf{u}$ are discretized using Adams-Bashforth, where $\mathbf{u}^{AB} = \mathbf{u}^n$ in the first time step and $\mathbf{u}^{AB} = 2\mathbf{u}^n - \mathbf{u}^{n-1}$ afterwards. As before, we use $\Delta t = \alpha\widehat{\Delta t}$ to simplify the equations.

In addition to these terms, $\mathbf{u}^v$ is an intermediate estimate of $\mathbf{u}^{n+1}$ using an approximation for pressure, which is computed in an intermediate implicit solve, and $\mathbf{m}$ is the total density flux detailed in Section 3.2.2. With these, (9) is discretized as

$$\frac{\rho^{n+1}\mathbf{u}^{n+1} - (\rho\mathbf{u})^{BD}}{\widehat{\Delta t}} + \nabla\cdot\left(\mathbf{m}\otimes\mathbf{u}^{AB}\right) = -\nabla p^{n+1} + \rho^{n+1}g + \sigma\kappa\nabla\left(g\left(\gamma^{n+1}\right)\right) + \nabla\cdot\left(\mu^{n+1}\left(\nabla\mathbf{u}^v + \left(\nabla\mathbf{u}^{AB}\right)^T\right)\right) + S_{\mathbf{u}}^{n+1}. \quad (30)$$

The intermediate $\mathbf{u}^*$ is introduced to represent the result of the momentum advection and also the evolution of density through the Cahn-Hilliard equation. When the Cahn-Hilliard equation causes mass to move around, the momentum carried by that mass must move with it. Otherwise mass and momentum may become inconsistent. Following [31] this is accomplished through the mass flux term $\mathbf{m}$, which we derive in Section 3.2.2.

$$\frac{\rho^{n+1}\mathbf{u}^* - (\rho\mathbf{u})^{BD}}{\widehat{\Delta t}} + \nabla\cdot\left(\mathbf{m}\otimes\mathbf{u}^{AB}\right) = 0 \quad (31)$$

$$\frac{\rho^{n+1}\mathbf{u}^{n+1} - \rho^{n+1}\mathbf{u}^*}{\widehat{\Delta t}} = -\nabla p^{n+1} + \rho^{n+1}g + \sigma\kappa\nabla\left(g\left(\gamma^{n+1}\right)\right) + \nabla\cdot\left(\mu^{n+1}\left(\nabla\mathbf{u}^v + \left(\nabla\mathbf{u}^{AB}\right)^T\right)\right) + S_{\mathbf{u}}^{n+1}. \quad (32)$$

After updating momentum according to equation (31), we divide the result through by ρ^{n+1} and formulate equation (32) as updates to velocity, beginning with explicit forces and pressure. We split pressure here into predicted and correction parts as $p^{n+1} = p^n + p'$.

$$\frac{\mathbf{u}^{**} - \mathbf{u}^*}{\widehat{\Delta t}} = -\frac{1}{\rho^{n+1}}\nabla p^n + g + \frac{1}{\rho^{n+1}}\sigma\kappa\nabla\left(g\left(\gamma^{n+1}\right)\right) + \frac{1}{\rho^{n+1}}\nabla\cdot\left(\mu^{n+1}\left(\nabla\mathbf{u}^{AB}\right)^T\right) + \frac{1}{\rho^{n+1}}S_{\mathbf{u}}^{n+1} \quad (33)$$

$$\frac{\mathbf{u}^{n+1} - \mathbf{u}^{**}}{\widehat{\Delta t}} = -\frac{1}{\rho^{n+1}}\nabla p' + \frac{1}{\rho^{n+1}}\nabla\cdot\left(\mu^{n+1}\nabla\mathbf{u}^v\right) \quad (34)$$

Finally, we compute the effects of viscosity implicitly and then project the velocity to be divergence free:

$$\frac{\mathbf{u}^v - \mathbf{u}^{**}}{\widehat{\Delta t}} = \frac{1}{\rho^{n+1}}\nabla\cdot\left(\mu^{n+1}\nabla\mathbf{u}^v\right) \quad (35)$$

$$\nabla\cdot\left(\frac{1}{\rho^{n+1}}\nabla p'\right) = \frac{\nabla\cdot\mathbf{u}^v}{\widehat{\Delta t}} \quad (36)$$

$$\frac{\mathbf{u}^{n+1} - \mathbf{u}^v}{\widehat{\Delta t}} = -\frac{1}{\rho^{n+1}}\nabla p'. \quad (37)$$

3.2.2. Momentum flux

Since we are solving the Cahn-Hilliard equation, we do not directly evolve density. Instead, $\gamma^n \to \gamma^{n+1}$ is evolved according to the Cahn-Hilliard equation, and then (5) is used to compute ρ^{n+1}. The discrete γ evolution in Section 3.1.1 implies a density evolution of the form

$$\frac{\rho^{n+1} - \rho^{BD}}{\widehat{\Delta t}} + \nabla\cdot\mathbf{m} = S_m^{n+1}, \quad (38)$$

where $\mathbf{m}$ includes advection and Cahn-Hilliard separation, and S_m takes the effects of the forcing term S_γ. Using (5), we express $\mathbf{m}$ in terms of γ:

$$\nabla\cdot\mathbf{m} = -\frac{\rho^{n+1} - \rho^{BD}}{\widehat{\Delta t}} + S_m^{n+1} \quad (39)$$

$$= -(\rho_1 - \rho_0)\frac{\gamma^{n+1} - \gamma^{BD}}{\widehat{\Delta t}} + S_m^{n+1} \quad (40)$$

$$= -(\rho_1 - \rho_0)\left(\frac{\gamma^{n+1} - \hat{\gamma}^{n+1}}{\widehat{\Delta t}} + \frac{\hat{\gamma}^{n+1} - \gamma'}{\widehat{\Delta t}} + \frac{\gamma' - \gamma^*}{\widehat{\Delta t}} + \frac{\gamma^* - \gamma^{BD}}{\widehat{\Delta t}}\right) + S_m^{n+1}. \quad (41)$$

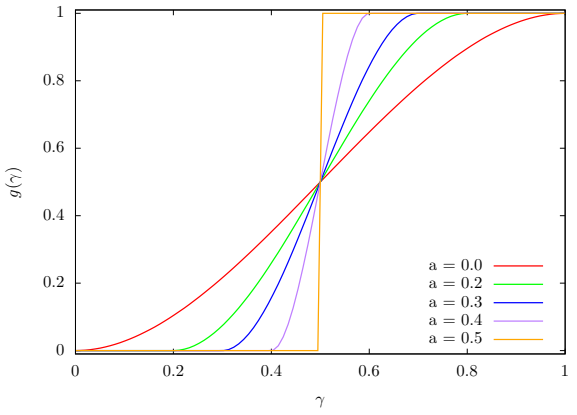

Fig. 1: $g(\gamma)$ vs γ for different values of a

Using the update rules (12), (19), (18), and (23), defining $S_m^{n+1} = (\rho_1 - \rho_0)\, S_\gamma^{n+1}$, and canceling terms, this becomes

$$\nabla \cdot \mathbf{m} = (\rho_1 - \rho_0)\left(\nabla \cdot \left(\mathbf{u}^{AB}\gamma^{AB}\right) - \nabla \cdot \left(s\nabla\gamma' + s\nabla\hat{\gamma}^{n+1} + W_b\left(\gamma^{n+1}\right)\nabla Q\right)\right) \tag{42}$$

Note that this definition of $\mathbf{m}$ is only well-defined up to a divergence-free shift. To determine what shift is necessary, we consider the case of $\rho_0 = \rho_1$, in which case Cahn-Hilliard has no affect on the density evolution and the mass flux is purely comprised of advection. This suggests the shift $\nabla \cdot \left(\rho_0 \mathbf{u}^{AB}\right)$ so that

$$\nabla \cdot \mathbf{m} = \nabla \cdot \left(\rho_0 \mathbf{u}^{AB}\right) + (\rho_1 - \rho_0)\left(\nabla \cdot \left(\mathbf{u}^{AB}\gamma^{AB}\right) - \nabla \cdot \left(s\nabla\gamma' + s\nabla\hat{\gamma}^{n+1} + W_b\left(\gamma^{n+1}\right)\nabla Q\right)\right), \tag{43}$$

which is consistent with the shift in [31]. Observe that ρ_0 is a constant and $\mathbf{u}^{AB}$ is discretely divergence free, so adding this term does not affect the value of $\nabla \cdot \mathbf{m}$. This leads to a definition of

$$\mathbf{m} = \rho_0 \mathbf{u}^{AB} + (\rho_1 - \rho_0)\left(\mathbf{u}^{AB}\gamma^{AB} - s\nabla\gamma' - s\nabla\hat{\gamma}^{n+1} - W_b\left(\gamma^{n+1}\right)\nabla Q\right). \tag{44}$$

To ensure consistency with the discretization of the Cahn-Hilliard equation, $\mathbf{u}^{AB}\gamma^{AB}$ is replaced by the flux computed by the WENO advection described in Section 3.3.

3.2.3. Surface tension discretization

For surface tension, we use a Continuum Surface Force [6, 18] formulation:

$$\sigma\kappa\nabla(g(\gamma)), \tag{45}$$

where κ is the estimated interface curvature:

$$\kappa = -\nabla \cdot \left(\frac{\nabla\gamma}{||\nabla\gamma||}\right). \tag{46}$$

We formulate $g(\gamma)$ to ensure that the surface tension force has finite support about the interface value $\gamma = 0.5$. In particular, for some value $a \in [0, 0.5]$, the surface tension force is exactly 0 for $\gamma \notin [a, 1-a]$. We choose a piecewise cubic approximation of a Heaviside function for $g(\gamma)$ whose transition occurs between a and $1-a$. Since $g(\gamma)$ approximates a Heaviside function, $\nabla g(\gamma)$ approximates a delta function times the normal. This is similar to the method used in [40], but it differs in that they use a level set function to track the interface rather than the phase-field approach used here and in the choice of Heaviside approximation.

As depicted in Figure 1, we define $g(\gamma)$ as

$$g(\gamma) = \begin{cases} 1, & \text{if } \gamma \geq 1-a \\ 0, & \text{if } \gamma < a \\ \frac{(-\gamma+a)^2(2\gamma+4a-3)}{(2a-1)^3}, & \text{otherwise.} \end{cases} \tag{47}$$

In practice, we've found $a = 0.2$ works well, and at $a = 0.5$ we recover a sharp interface force, as used in [34].

We can see that this surface tension formulation is consistent with the standard one by considering a path that crosses the band near the interface where the force is nonzero. Given any path C (see Figure 2), with discretization $i = 0, ..., N$, that crosses the fluid interface, the total force per unit area is:

$$\int_C \sigma\kappa\nabla g(\gamma)\cdot dl \approx \sigma\left(\sum_{i=1}^{N}\kappa_i\left(g(\gamma_i)-g(\gamma_{i-1})\right)\right). \tag{48}$$

Assume that $g(\gamma_N) = 1$ and $g(\gamma_0) = 0$, so that the curve crosses completely from one phase to the other. Let κ_I denote the curvature at the interface. If we assume the path is localized and approximate the curvature as constant, so that $\kappa_i = \kappa_I$, (48) reduces to:

$$\sigma\left(\sum_{i=1}^{N}\kappa_i\left(g(\gamma_i)-g(\gamma_{i-1})\right)\right) = \sigma\kappa_I\left(g(\gamma_N)-g(\gamma_0)\right) = \sigma\kappa_I, \tag{49}$$

which is the ideal pressure jump caused by surface tension. In reality, the curvature will not be constant, but when the interface width is small and the curvature is sufficiently smooth, we can write $\kappa_i = \kappa_I + O(\Delta x)$, so that the approximate pressure jump is

$$\sigma\left(\sum_{i=1}^{N}\kappa_i\left(g(\gamma_i)-g(\gamma_{i-1})\right)\right) = \sigma\kappa_I + O(\Delta x). \tag{50}$$

This suggests that smearing the pressure jump over a transition region using $g(\gamma)$ can give a consistent discretization of the surface tension force. We next show this explicitly for our discretization of the pressure Poisson equation (36).

For the pressure projection equation, we solve $\nabla\cdot(\beta\nabla p') = \nabla\cdot\mathbf{u}^v$ with $\beta = \frac{\widehat{\Delta t}}{\rho^{n+1}}$. The standard five-point discretization of this equation in two dimensions is given by

$$\frac{\beta_{i+\frac{1}{2},j}\left(p'_{i+1,j}-p'_{i,j}\right)-\beta_{i-\frac{1}{2},j}\left(p'_{i,j}-p'_{i-1,j}\right)}{\Delta x^2}+\frac{\beta_{i,j+\frac{1}{2}}\left(p'_{i,j+1}-p'_{i,j}\right)-\beta_{i,j-\frac{1}{2}}\left(p'_{i,j}-p'_{i,j-1}\right)}{\Delta y^2} = (\nabla\cdot\mathbf{u}^v)_{i,j}. \tag{51}$$

Following [34], an interface can be treated in a sharp manner by incorporating the pressure jump J across the interface into the equation. Incorporating a jump term (which may be 0) across every difference in the stencil, the discretization becomes

$$\begin{aligned}&\frac{\beta_{i+\frac{1}{2},j}\left(p'_{i+1,j}-\left(p'_{i,j}+J_{i+\frac{1}{2},j}\right)\right)-\beta_{i-\frac{1}{2},j}\left(p'_{i,j}-\left(p'_{i-1,j}+J_{i-\frac{1}{2},j}\right)\right)}{\Delta x^2}\\ &+\frac{\beta_{i,j+\frac{1}{2}}\left(p'_{i,j+1}-\left(p'_{i,j}+J_{i,j+\frac{1}{2}}\right)\right)-\beta_{i,j-\frac{1}{2}}\left(p'_{i,j}-\left(p'_{i,j-1}+J_{i,j-\frac{1}{2}}\right)\right)}{\Delta y^2} = (\nabla\cdot\mathbf{u}^v)_{i,j}.\end{aligned} \tag{52}$$

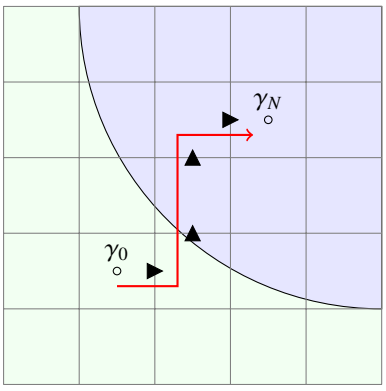

Fig. 2: Example path $\gamma_0 \to \gamma_N$. The triangles represent the pressure jumps along this path.

Moving all terms with jumps to the right hand side, we get

$$\begin{aligned}\frac{\beta_{i+\frac{1}{2},j}\left(p'_{i+1,j}-p'_{i,j}\right)-\beta_{i-\frac{1}{2},j}\left(p'_{i,j}-p'_{i-1,j}\right)}{\Delta x^2}+\frac{\beta_{i,j+\frac{1}{2}}\left(p'_{i,j+1}-p'_{i,j}\right)-\beta_{i,j-\frac{1}{2}}\left(p'_{i,j}-p'_{i,j-1}\right)}{\Delta y^2}\\ =\left(\nabla\cdot\mathbf{u}^v\right)_{i,j}+\frac{\beta_{i+\frac{1}{2},j}J_{i+\frac{1}{2},j}-\beta_{i-\frac{1}{2},j}J_{i-\frac{1}{2},j}}{\Delta x^2}+\frac{\beta_{i,j+\frac{1}{2}}J_{i,j+\frac{1}{2}}-\beta_{i,j-\frac{1}{2}}J_{i,j-\frac{1}{2}}}{\Delta y^2}.\end{aligned} \tag{53}$$

With the central difference discretization of divergence

$$\left(\nabla\cdot\mathbf{u}^v\right)_{i,j}=\frac{u^v_{i+\frac{1}{2},j}-u^v_{i-\frac{1}{2},j}}{\Delta x}+\frac{v^v_{i,j+\frac{1}{2}}-v^v_{i,j-\frac{1}{2}}}{\Delta y}, \tag{54}$$

and with $\hat{\mathbf{J}}=\left(\frac{J_x}{\Delta x},\frac{J_y}{\Delta y}\right)$, Equation (53) becomes

$$\frac{\beta_{i+\frac{1}{2},j}\left(p'_{i+1,j}-p'_{i,j}\right)-\beta_{i-\frac{1}{2},j}\left(p'_{i,j}-p'_{i-1,j}\right)}{\Delta x^2}+\frac{\beta_{i,j+\frac{1}{2}}\left(p'_{i,j+1}-p'_{i,j}\right)-\beta_{i,j-\frac{1}{2}}\left(p'_{i,j}-p'_{i,j-1}\right)}{\Delta y^2}=\left(\nabla\cdot\left(\mathbf{u}^v+\beta\hat{\mathbf{J}}\right)\right)_{i,j}. \tag{55}$$

We define the pressure jump at $\left(i+\frac{1}{2},j\right)$ to be

$$J_{i+\frac{1}{2},j}=\sigma\kappa_{i+\frac{1}{2},j}\left(g\left(\gamma_{i+1,j}\right)-g\left(\gamma_{i,j}\right)\right). \tag{56}$$

The discretization of the x component of the surface tension force (45) is then

$$\sigma\kappa_{i+\frac{1}{2},j}\left(\frac{\partial g}{\partial x}\left(\gamma\right)\right)_{i+\frac{1}{2},j}\approx\sigma\kappa_{i+\frac{1}{2},j}\frac{g\left(\gamma_{i+1,j}\right)-g\left(\gamma_{i,j}\right)}{\Delta x}=\frac{1}{\Delta x}J_{i+\frac{1}{2},j}, \tag{57}$$

which is similar to [18]. Therefore

$$\beta\hat{\mathbf{J}}=\frac{\widehat{\Delta t}}{\rho^{n+1}}\sigma\kappa\nabla g\left(\gamma\right), \tag{58}$$

which shows that solving the Poisson equation with the above defined pressure jumps is equivalent to applying surface tension with other explicit forces:

$$\nabla\cdot\left(\frac{\widehat{\Delta t}}{\rho^{n+1}}\nabla p'\right)=\nabla\cdot\left(\mathbf{u}^v+\frac{\widehat{\Delta t}}{\rho^{n+1}}\sigma\kappa\nabla g\left(\gamma\right)\right). \tag{59}$$

Therefore we apply surface tension as in (59), and we can recover the sharp formulation of [34] by choosing $a=0.5$ in the definition of $g\left(\gamma\right)$.

3.3. Spatial Discretization

We use a uniform MAC grid (Figure 3) with γ and pressure stored at cell centers. Velocities are split by components and stored on cell faces. Unless otherwise specified, all divergences are central differences from faces to cells and all gradients are central differences from cells to faces. All Poisson equations are discretized using the standard five-point central difference stencil, with standard treatment of axis-aligned boundary conditions.

3.3.1. Advective flux for γ

When computing the divergence operator for γ advection in (12), we use a flux-based 5th order WENO advection scheme [33] with local Lax-Friedrichs [56]. The WENO flux $\mathcal{F}^W$ is stored for later use in the momentum flux $\mathbf{m}$.

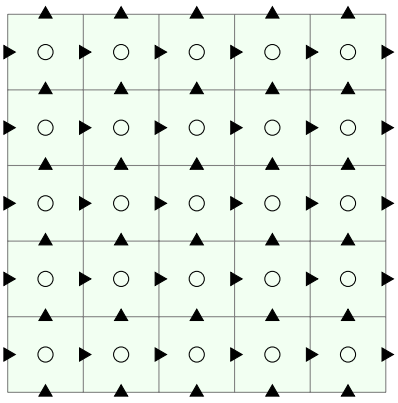

Fig. 3: The MAC grid stores velocQities on faces (represented by triangles), and γ and pressure on cell centers (circles).

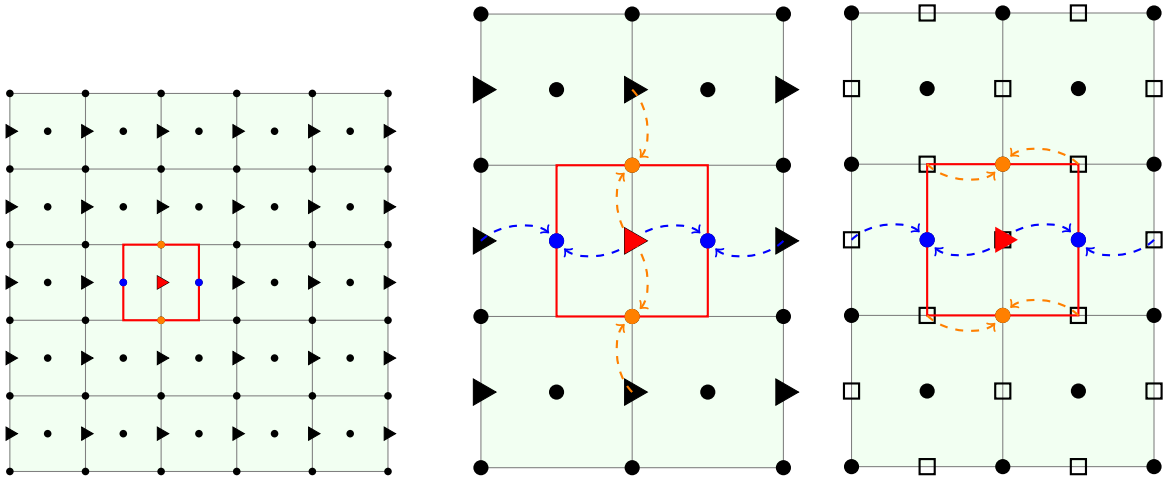

(a) Flux locations around u component. (b) u component interpolation for flux. (c) $\mathbf{m}^x$ component interpolation for flux.

Fig. 4: The components of the momentum flux for updating the x component of momentum in 2D are shown in 4a. The momentum at the red triangle will be updated with the fluxes at the surrounding blue and orange dots. The u and $\mathbf{m}^x$ values at these dots are interpolated from neighboring values as illustrated in 4b and 4c, respectively.

3.3.2. Divergence operator (momentum advection)

The divergence operator for momentum advection is discretized as a central difference from dual-cell faces to MAC grid faces, as shown in Figure 4. The components of the divergence $\nabla \cdot (\mathbf{m} \otimes \mathbf{u})$ are needed at MAC faces to update the components of our velocities. Correspondingly we discretize $\nabla \cdot (\mathbf{m}^x u)$ and $\nabla \cdot (\mathbf{m}^y v)$ at MAC x-faces and y-faces respectively. For example, $\mathbf{m}^x$ is interpolated to faces of a uniform dual grid centered on the x-faces:

$$\mathbf{m}^x_{i,j} = \frac{\mathbf{m}_{i+1/2,j} + \mathbf{m}_{i-1/2,j}}{2} \tag{60}$$

$$\mathbf{m}^x_{i+1/2,j+1/2} = \frac{\mathbf{m}_{i+1,j+1/2} + \mathbf{m}_{i,j+1/2}}{2}. \tag{61}$$

We also interpolate u to the same dual grid faces

$$u_{i,j} = \frac{u_{i+1/2,j} + u_{i-1/2,j}}{2} \tag{62}$$

$$u_{i+1/2,j+1/2} = \frac{u_{i+1/2,j+1} + u_{i+1/2,j}}{2}. \tag{63}$$

The final component divergence is discretized as

$$(\nabla \cdot (\mathbf{m}^x u))_{i+1/2,j} = \frac{\mathbf{m}^x_{i+1,j} u_{i+1,j} - \mathbf{m}^x_{i,j} u_{i,j}}{\Delta x} + \frac{\mathbf{m}^x_{i+1/2,j+1/2} u_{i+1/2,j+1/2} - \mathbf{m}^x_{i+1/2,j-1/2} u_{i+1/2,j-1/2}}{\Delta y}. \tag{64}$$

The $\mathbf{m}^y$ term is discretized analogously.

3.3.3. Divergence gradient transpose

In (33), we discretize the $\nabla \cdot \left(\mu (\nabla \mathbf{u})^T\right)$ term following [31], which we show here:

$$\begin{aligned}
\left(\nabla \cdot \left(\mu (\nabla \mathbf{u})^T\right)\right)_{i,j} = & \frac{1}{\Delta x}\left(\mu_{i+1/2,j} \frac{u_{i+1,j} - u_{i,j}}{\Delta x} - \mu_{i-1/2,j} \frac{u_{i,j} - u_{i-1,j}}{\Delta x}\right) \\
& + \frac{1}{\Delta y}\left(\mu_{i,j+1/2} \frac{v_{i+1/2,j+1/2} - v_{i-1/2,j+1/2}}{\Delta x} - \mu_{i,j-1/2} \frac{v_{i+1/2,j-1/2} - v_{i-1/2,j-1/2}}{\Delta x}\right) \\
& + \frac{1}{\Delta y}\left(\mu_{i,j+1/2} \frac{v_{i,j+1} - v_{i,j}}{\Delta y} - \mu_{i,j-1/2} \frac{v_{i,j} - v_{i,j-1}}{\Delta y}\right) \\
& + \frac{1}{\Delta x}\left(\mu_{i+1/2,j} \frac{u_{i+1/2,j+1/2} - u_{i+1/2,j-1/2}}{\Delta y} - \mu_{i-1/2,j} \frac{u_{i-1/2,j+1/2} - u_{i-1/2,j-1/2}}{\Delta y}\right).
\end{aligned} \tag{65}$$

This discretization is used to ensure discrete consistency when μ is constant, such that

$$\nabla \cdot \left(\mu (\nabla \mathbf{u})^T\right) = \mu \nabla (\nabla \cdot \mathbf{u}) = 0 \tag{66}$$

is satisfied and momentum is conserved [31].

3.3.4. Interface curvature

The Balanced-Force algorithm [18] requires that the surface tension force is discretized at the same spatial location as the pressure gradient. When calculating the estimated interface curvature κ,

$$\kappa = -\nabla \cdot \left(\frac{\nabla \gamma}{||\nabla \gamma||}\right), \tag{67}$$

we smooth the curvature estimate by computing the divergence on cells and interpolating to faces. We calculate $\nabla \gamma$ as individual components $\nabla \gamma^x, \nabla \gamma^y$ on faces,

$$\nabla \gamma^x_{i+1/2,j} = \frac{\gamma_{i+1,j} - \gamma_{i,j}}{\Delta x}, \tag{68}$$

which we interpolate to cell centers as vectors in order to normalize:

$$\widetilde{\nabla \gamma}_{i,j} = \left(\frac{\nabla \gamma^x_{i+1/2,j} + \nabla \gamma^x_{i-1/2,j}}{2}, \frac{\nabla \gamma^y_{i,j+1/2} + \nabla \gamma^y_{i,j-1/2}}{2}\right). \tag{69}$$

The normalized gradients are interpolated back to faces as full vectors:

$$\widehat{\nabla \gamma}_{i+1/2,j} = \frac{1}{2}\left(\frac{\widetilde{\nabla \gamma}_{i+1,j}}{||\widetilde{\nabla \gamma}_{i+1,j}||} + \frac{\widetilde{\nabla \gamma}_{i,j}}{||\widetilde{\nabla \gamma}_{i,j}||}\right). \tag{70}$$

From these gradient vectors on faces, we calculate the divergence at cell centers

$$\nabla \cdot \left(\widehat{\nabla \gamma}\right)_{i,j} = \frac{1}{\Delta x}\left(\widehat{\nabla \gamma}^x_{i+1/2,j} - \widehat{\nabla \gamma}^x_{i-1/2,j}\right) + \frac{1}{\Delta y}\left(\widehat{\nabla \gamma}^y_{i,j+1/2} - \widehat{\nabla \gamma}^y_{i,j-1/2}\right), \tag{71}$$

and interpolate to faces:

$$\kappa_{i+1/2,j} = -\frac{\nabla \cdot \left(\widehat{\nabla \gamma}\right)_{i+1,j} + \nabla \cdot \left(\widehat{\nabla \gamma}\right)_{i,j}}{2}. \tag{72}$$

3.4. Discretization summary

We finish our treatment of discretization with a summary of the full algorithm. First, the Adams-Bashforth and backwards-difference quantities γ^{BD} and γ^{AB} on cell centers and $(\rho\mathbf{u})^{BD}$ and $\mathbf{u}^{AB}$ on cell faces are computed from the known initial quantities and previous time step quantities. The initial time step is computed with first order time discretizations:

$$\gamma^{BD} = \gamma^n \qquad \gamma^{AB} = \gamma^n \qquad (\rho\mathbf{u})^{BD} = \rho^n\mathbf{u}^n \qquad \mathbf{u}^{AB} = \mathbf{u}^n \qquad \widehat{\Delta t} = \Delta t, \tag{73}$$

and successive time steps with second order:

$$\gamma^{BD} = \frac{4}{3}\gamma^n - \frac{1}{3}\gamma^{n-1} \quad \gamma^{AB} = 2\gamma^n - \gamma^{n-1} \quad (\rho\mathbf{u})^{BD} = \frac{4}{3}\rho^n\mathbf{u}^n - \frac{1}{3}\rho^{n-1}\mathbf{u}^{n-1} \quad \mathbf{u}^{AB} = 2\mathbf{u}^n - \mathbf{u}^{n-1} \quad \widehat{\Delta t} = \frac{2}{3}\Delta t. \tag{74}$$

3.4.1. Cahn-Hilliard discretization

Unlike [31], we observed better results using a WENO advection scheme (Section 3.3.1) to compute γ^* from γ^{BD}. The flux $\mathcal{F}^W$ from this operation is stored for later use in $\mathbf{m}$. These terms are related by:

$$\gamma^*_{i,j} = \gamma^{BD}_{i,j} - \widehat{\Delta t}\left(\frac{\mathcal{F}^W_{i+1/2,j} - \mathcal{F}^W_{i-1/2,j}}{\Delta x} + \frac{\mathcal{F}^W_{i,j+1/2} - \mathcal{F}^W_{i,j-1/2}}{\Delta y}\right). \tag{75}$$

Next we compute $\hat{\gamma}^{n+1}$ from γ^* by solving two Helmholtz equations:

$$\lambda = \frac{3}{2\sqrt{2}}\sigma\eta \qquad s = \sqrt{\frac{M\lambda}{\widehat{\Delta t}}} \qquad A = \frac{M\lambda}{s}F'\left(\gamma^{AB}\right) - 2\gamma^{AB} \tag{76}$$

$$\gamma' - s\widehat{\Delta t}\nabla^2\gamma' = \gamma^* + A + \widehat{\Delta t}S_\gamma^{n+1} \tag{77}$$

$$\hat{\gamma}^{n+1} - s\widehat{\Delta t}\nabla^2\hat{\gamma}^{n+1} = \gamma' - A. \tag{78}$$

We obtain the final γ^{n+1} through the redistribution scheme described in Section 3.1.2. The flux corresponding to the redistribution is found with a Poisson solve:

$$\gamma^{b*}_{i,j} = \begin{cases} 1, & \text{if } \hat{\gamma}^{n+1}_{i,j} \geq 1 \\ 0, & \text{if } \hat{\gamma}^{n+1}_{i,j} \leq 0 \\ \hat{\gamma}^{n+1}_{i,j}, & \text{otherwise.} \end{cases} \tag{79}$$

$$W_b(\gamma) = 4\gamma - 4\gamma^2 \tag{80}$$

$$\gamma^{n+1}_{i,j} = \gamma^{b*}_{i,j} + \frac{W_b\left(\gamma^{b*}_{i,j}\right)}{\sum\limits_{r,s} W_b\left(\gamma^{b*}_{r,s}\right)} \sum_{r,s}\left(\hat{\gamma}^{n+1}_{r,s} - \gamma^{b*}_{r,s}\right) \tag{81}$$

$$\widehat{\Delta t}\nabla\cdot\left(W_b\left(\gamma^{n+1}\right)\nabla Q\right) = \gamma^{n+1} - \hat{\gamma}^{n+1}. \tag{82}$$

To avoid rows of all zeros in our Poisson matrix, we follow [30] in replacing $W_b\left(\gamma^{n+1}\right)$ with $\max\left(W_b\left(\gamma^{n+1}\right), 10^{-6}\right)$ in (82). Using the above, we can compute the discrete mass flux, which should satisfy (38) to round-off error:

$$\mathbf{m} = \rho_0\mathbf{u}^{AB} + (\rho_1 - \rho_0)\left(\mathcal{F}^W - s\nabla\gamma' - s\nabla\hat{\gamma}^{n+1} - W_b\left(\gamma^{n+1}\right)\nabla Q\right). \tag{83}$$

The density and viscosity are computed on faces using γ^{n+1} that has been linearly interpolated to faces:

$$\rho^{n+1} = \rho_0 + (\rho_1 - \rho_0)\,\gamma^{n+1} \tag{84}$$

$$\mu^{n+1} = \mu_0 + (\mu_1 - \mu_0)\,\gamma^{n+1}. \tag{85}$$

3.4.2. Navier-Stokes discretization

We first update the momentum to be consistent with the movement of mass that occurred due to the Cahn-Hilliard equation by:

$$\rho^{n+1}\mathbf{u}^* = (\rho\mathbf{u})^{BD} - \widehat{\Delta t}\nabla\cdot\left(\mathbf{m}\otimes\mathbf{u}^{AB}\right), \tag{86}$$

after which ρ^{n+1} is divided off to obtain $\mathbf{u}^*$. Next we apply explicit forces:

$$\mathbf{u}^{**} = \mathbf{u}^* + \widehat{\Delta t}\mathbf{g} + \frac{\widehat{\Delta t}}{\rho^{n+1}}\left(\sigma\kappa\nabla\left(g\left(\gamma^{n+1}\right)\right)\right) + \frac{\widehat{\Delta t}}{\rho^{n+1}}\nabla\cdot\left(\mu^{n+1}\left(\nabla\mathbf{u}^{AB}\right)^T\right) - \frac{\widehat{\Delta t}}{\rho^{n+1}}\nabla p^n + \widehat{\Delta t}S_{\mathbf{u}}^{n+1} \tag{87}$$

where

$$\kappa = -\nabla\cdot\left(\frac{\nabla\gamma}{||\nabla\gamma||}\right) \tag{88}$$

$$g(\gamma) = \begin{cases} 1, & \text{if } \gamma \geq 1-a \\ 0, & \text{if } \gamma < a \\ \frac{(-\gamma+a)^2(2\gamma+4a-3)}{(2a-1)^3}, & \text{otherwise} \end{cases} \tag{89}$$

We use $a = 0.2$ unless otherwise stated. We solve the viscosity equation for each component of $\mathbf{u}^v$ by solving a Helmholtz equation:

$$\mathbf{u}^v - \frac{\widehat{\Delta t}}{\rho^{n+1}}\nabla\cdot\left(\mu^{n+1}\nabla\mathbf{u}^v\right) = \mathbf{u}^{**}. \tag{90}$$

The pressure correction is obtained by solving the Poisson equation:

$$\nabla\cdot\left(\frac{\widehat{\Delta t}}{\rho^{n+1}}\nabla p'\right) = \nabla\cdot\mathbf{u}^v \tag{91}$$

$$p^{n+1} = p^n + p', \tag{92}$$

and the pressure correction is applied to obtain the final velocity:

$$\mathbf{u}^{n+1} = \mathbf{u}^v - \frac{\widehat{\Delta t}}{\rho^{n+1}}\nabla p'. \tag{93}$$

4. Analysis

4.1. Von Neumann stability analysis

We can get a sense of the stability of the Cahn-Hilliard discretization by performing von Neumann analysis. To do this, we must first identify nonlinearities. The first is advection, which uses conservative WENO and has a CFL restriction; we must ensure $|u|\Delta t \leq \Delta x$, which we always obey. In the analysis that follows, we ignore advection by assuming zero velocity and also ignore redistribution. The other nonlinearity we must address is the double-well potential, which we replace by a single-well potential, so that $F'(\gamma) = k\gamma$, for $k > 0$.

With the nonlinearities eliminated, we may assume periodic boundary conditions and perform von Neumann analysis. To do this, we assume a solution of the form $\gamma_{r,s}^n = g^n e^{ia\Delta xr + ib\Delta xs}$, where a and b are the wave numbers of the solution and g is the (potentially complex-valued) growth factor. Note that g^n is g to the n-th power. The scheme is

stable if $|g| < 1$ and unstable if $|g| > 1$; the case $|g| = 1$ is more complex but not of importance here.

$$\gamma_{r,s}^{n} = g^n e^{ia\Delta xr + ib\Delta xs} \tag{94}$$

$$\gamma_{r,s}^{n-1} = g^{n-1} e^{ia\Delta xr + ib\Delta xs} \tag{95}$$

$$\gamma_{r,s}^{BD} = \frac{4}{3}\gamma_{r,s}^{n} - \frac{1}{3}\gamma_{r,s}^{n-1} = c_0 g^n e^{ia\Delta xr + ib\Delta xs} \qquad c_0 = \frac{4}{3} - \frac{1}{3g} \tag{96}$$

$$\gamma_{r,s}^{AB} = 2\gamma_{r,s}^{n} - \gamma_{r,s}^{n-1} = c_1 g^n e^{ia\Delta xr + ib\Delta xs} \qquad c_1 = 2 - \frac{1}{g} \tag{97}$$

$$\gamma_{r,s}^{*} = \gamma_{r,s}^{BD} = c_0 g^n e^{ia\Delta xr + ib\Delta xs} \tag{98}$$

$$A_{r,s} = \frac{M\lambda}{s} k\gamma^{AB} - 2\gamma^{AB} = c_2 g^n e^{ia\Delta xr + ib\Delta xs} \qquad c_2 = \left(\frac{M\lambda}{s}k - 2\right) c_1 \tag{99}$$

$$B_{r,s} = \gamma_{r,s}^{*} + A_{r,s} = c_3 g^n e^{ia\Delta xr + ib\Delta xs} \qquad c_3 = c_0 + c_2 \tag{100}$$

$$\gamma'_{r,s} = c_4 g^n e^{ia\Delta xr + ib\Delta xs} \tag{101}$$

$$B_{r,s} = \gamma'_{r,s} - s\widehat{\Delta t}\nabla^2 \gamma'_{r,s} \tag{102}$$

$$B_{r,s} = \gamma'_{r,s} - s\widehat{\Delta t}\frac{\gamma'_{r+1,s} + \gamma'_{r-1,s} + \gamma'_{r,s+1} + \gamma'_{r,s-1} - 4\gamma'_{r,s}}{\Delta x^2} \qquad c_3 = c_4\left(1 - s\frac{\widehat{\Delta t}}{\Delta x^2}\left(e^{ia\Delta x} + e^{-ia\Delta x} + e^{ib\Delta x} + e^{-ib\Delta x} - 4\right)\right) \tag{103}$$

$$C_{r,s} = \gamma'_{r,s} - A_{r,s} = c_5 g^n e^{ia\Delta xr + ib\Delta xs} \qquad c_5 = c_4 - c_2 \tag{104}$$

$$\gamma_{r,s}^{n+1} = g^{n+1} e^{ia\Delta xr + ib\Delta xs} \tag{105}$$

$$C_{r,s} = \hat{\gamma}_{r,s}^{n+1} - s\widehat{\Delta t}\nabla^2 \hat{\gamma}_{r,s}^{n+1} \tag{106}$$

$$C_{r,s} = \gamma_{r,s}^{n+1} - s\widehat{\Delta t}\frac{\gamma_{r+1,s}^{n+1} + \gamma_{r-1,s}^{n+1} + \gamma_{r,s+1}^{n+1} + \gamma_{r,s-1}^{n+1} - 4\gamma_{r,s}^{n+1}}{\Delta x^2} \qquad c_5 = g\left(1 - s\frac{\widehat{\Delta t}}{\Delta x^2}\left(e^{ia\Delta x} + e^{-ia\Delta x} + e^{ib\Delta x} + e^{-ib\Delta x} - 4\right)\right) \tag{107}$$

Combining the equations relating the constants $c_0, \ldots, c_5$, we obtain an equation for g. To simplify the algebra, we let $q = 4 - e^{ia\Delta x} - e^{-ia\Delta x} - e^{ib\Delta x} - e^{-ib\Delta x}$, so that $0 \le q \le 8$. We eliminate M and λ using $M\lambda = s^2\widehat{\Delta t}$. Our equations then become

$$c_0 = \frac{4}{3} - \frac{1}{3g} \qquad c_1 = 2 - \frac{1}{g} \qquad c_2 = \left(s\widehat{\Delta t}k - 2\right)c_1 \qquad c_3 = c_0 + c_2 \tag{108}$$

$$c_3 = c_4\left(1 + s\frac{\widehat{\Delta t}}{\Delta x^2}q\right) \qquad c_5 = c_4 - c_2 \qquad c_5 = g\left(1 + s\frac{\widehat{\Delta t}}{\Delta x^2}q\right) \tag{109}$$

We can further simplify these with $m = s\frac{\widehat{\Delta t}}{\Delta x^2}q$ and $p = s\widehat{\Delta t}k$, where $m \ge 0$ and $p > 0$. Combining these leads to the quadratic equation

$$3g^2(1+m)^2 + (6mp - 12m - 4)g - 3mp + 6m + 1 = 0. \tag{110}$$

We must show that this equation never has a root with $|g| > 1$. At $m = 0$, we have $3g^2 - 4g + 1 = 0$, which has solutions $g = 1, \frac{1}{3}$. Solving (110) using the quadratic formula and taking a Taylor series in m we see that $g = 1 - \frac{3}{2}mp + O(m^2)$, so that if m is positive but sufficiently small, we have real g with $0 < g < 1$. Next, we must show that if m continues to increase, we continue to have $|g| < 1$. If we were to violate this as we increase m, then for some m we must have (a) $g = 1$, (b) $g = -1$, or (c) g is a complex conjugate pair with $|g| = 1$. We consider each possibility in turn. For case (a), we let $g = 1$ in (110), which yields $3m(m + p) = 0$, which is impossible for $m > 0$ and $p > 0$.

For case (c), note that if $g^2 + rg + s = 0$ has complex conjugate roots, then $|g|^2 = g\overline{g} = s$, so that

$$|g|^2 = \frac{-3mp + 6m + 1}{3(1+m)^2} \le \frac{6m+1}{3(1+m)^2} = \frac{6m+1}{(6m+1) + (2+3m^2)} < 1. \tag{111}$$

Finally, we conclude that any instability (and thus time step restriction) must occur as a result of case (b). For case (b), we plug $g = -1$ into (110), which yields

$$3m^2 - 9mp + 24m + 8 = 0. \tag{112}$$

Plugging in m and p, eliminating s (which depends on $\widehat{\Delta t}$), and simplifying yields

$$3q(q - 3k\Delta x^2)\left(\frac{\sqrt{\widehat{\Delta t}M\lambda}}{\Delta x^2}\right)^2 + 24q\left(\frac{\sqrt{\widehat{\Delta t}M\lambda}}{\Delta x^2}\right) + 8 = 0, \tag{113}$$

which is a quadratic polynomial in $\sqrt{\widehat{\Delta t}}$. If $q - 3k\Delta x^2 \geq 0$, all of the coefficients of the polynomial will be positive, so that no positive roots can exist. Thus, we must have $q - 3k\Delta x^2 < 0$. Let $q = 3fk\Delta x^2$, where $0 < f < 1$. (Note that the entire range of f might not be feasible, since it may violate $q \leq 8$, but for Δx sufficiently small this will not be the case.) This leads to

$$27f(f-1)\left(k\sqrt{\widehat{\Delta t}M\lambda}\right)^2 + 72f\left(k\sqrt{\widehat{\Delta t}M\lambda}\right) + 8 = 0 \tag{114}$$

If $0 < f < 1$, this has one positive solution and one negative solution. The positive solution is

$$k\sqrt{\widehat{\Delta t}M\lambda} = \frac{2(6f + \sqrt{30f^2 + 6f})}{9f(1-f)} \tag{115}$$

Since we want the wavenumber leading to the tightest time step restriction, we choose f to minimize the right, which occurs at

$$f = \frac{\sqrt{6} - 1}{10} \approx 0.1449 \tag{116}$$

$$k\sqrt{\widehat{\Delta t}M\lambda} = \frac{24 + 4\sqrt{6}}{9} \approx 3.755 \tag{117}$$

This finally leads to the time step restriction

$$\Delta t \leq \frac{16(7 + 2\sqrt{6})}{9k^2M\lambda} \approx \frac{21.15}{k^2M\lambda}, \tag{118}$$

where we have used $\Delta t = \frac{3}{2}\hat{\Delta} t$. We note that the time step restriction on Δt is independent of Δx. We numerically evaluate the stability of the linearized stability analysis in Section 5.3.

4.2. Truncation error analysis

In this section, we compute the truncation error for the Cahn-Hilliard discretization. We omit advection from the analysis, since WENO advection is difficult to analyze and is more accurate than the rest of the scheme. We also omit spatial accuracy from the analysis, since all of the spatial stencils are second order accurate. Instead, we focus on the temporal accuracy. We compute the truncation error by plugging the analytical solution $\gamma(\mathbf{x}, t)$ into the discretization. Because of the Helmholtz solves, it is easiest to compute intermediates from the beginning and the end, measuring the error where they meet. We perform our Taylor expansion about the time $t = n + 1$ and in 1D for simplicity.

$$\gamma^{n+1} = \gamma \tag{119}$$

$$\gamma^{n} = \gamma - \Delta t\gamma_t + \frac{1}{2}\Delta t^2\gamma_{tt} + O(\Delta t^3) \tag{120}$$

$$\gamma^{n-1} = \gamma - 2\Delta t\gamma_t + 2\Delta t^2\gamma_{tt} + O(\Delta t^3) \tag{121}$$

$$\gamma^{*} = \gamma^{BD} = \frac{4}{3}\gamma^n - \frac{1}{3}\gamma^{n-1} = \gamma - \frac{2}{3}\Delta t\gamma_t + O(\Delta t^3) \tag{122}$$

$$\gamma^{AB} = 2\gamma^n - \gamma^{n-1} = \gamma - \Delta t^2\gamma_{tt} + O(\Delta t^3) \tag{123}$$

Next, we note that $\widehat{\Delta t} = \frac{2}{3}\Delta t$ and $s = \sqrt{\frac{M\lambda}{\widehat{\Delta t}}} = \sqrt{\frac{3M\lambda}{2}}\Delta t^{-1/2} = \hat{s}\Delta t^{-1/2}$, where we have introduced $\hat{s}$ to simplify the algebra.

$$A = \frac{M\lambda}{s}F'\left(\gamma^{AB}\right) - 2\gamma^{AB} \tag{124}$$

$$= \Delta t^{1/2}\frac{M\lambda}{\hat{s}}F'(\gamma) - \Delta t^{5/2}\frac{M\lambda}{\hat{s}}\gamma_{tt}F''(\gamma) - 2\gamma + 2\Delta t^2\gamma_{tt} + O(\Delta t^3) \tag{125}$$

$$= -2\gamma + \Delta t^{1/2}\frac{M\lambda}{\hat{s}}F'(\gamma) + 2\Delta t^2\gamma_{tt} - \Delta t^{5/2}\frac{M\lambda}{\hat{s}}\gamma_{tt}F''(\gamma) + O(\Delta t^3) \tag{126}$$

$$\gamma' = \gamma^{n+1} - s\widehat{\Delta t}\nabla^2\gamma^{n+1} + A \tag{127}$$

$$= \gamma - \frac{2}{3}\hat{s}\Delta t^{1/2}\gamma_{xx} + \Delta t^{1/2}\frac{M\lambda}{\hat{s}}F'(\gamma) - \Delta t^{5/2}\frac{M\lambda}{\hat{s}}\gamma_{tt}F''(\gamma) - 2\gamma + 2\Delta t^2\gamma_{tt} + O(\Delta t^3) \tag{128}$$

$$= -\gamma - \frac{2}{3}\hat{s}\Delta t^{1/2}\gamma_{xx} + \Delta t^{1/2}\frac{M\lambda}{\hat{s}}F'(\gamma) + 2\Delta t^2\gamma_{tt} - \Delta t^{5/2}\frac{M\lambda}{\hat{s}}\gamma_{tt}F''(\gamma) + O(\Delta t^3) \tag{129}$$

$$\gamma'_x = -\gamma_x - \frac{2}{3}\hat{s}\Delta t^{1/2}\gamma_{xxx} + \Delta t^{1/2}\frac{M\lambda}{\hat{s}}\gamma_x F''(\gamma) + 2\Delta t^2\gamma_{ttx} + O(\Delta t^{5/2}) \tag{130}$$

$$\gamma'_{xx} = -\gamma_{xx} - \frac{2}{3}\hat{s}\Delta t^{1/2}\gamma_{xxxx} + \Delta t^{1/2}\frac{M\lambda}{\hat{s}}\gamma_{xx}F''(\gamma) + \Delta t^{1/2}\frac{M\lambda}{\hat{s}}\gamma_x\gamma_x F'''(\gamma) + 2\Delta t^2\gamma_{ttxx} + O(\Delta t^{5/2}) \tag{131}$$

Finally, we compute the truncation error as

$$\delta = \gamma' - s\widehat{\Delta t}\nabla^2\gamma' - \gamma^* - A \tag{132}$$

$$= \gamma - \frac{2}{3}\hat{s}\Delta t^{1/2}\gamma_{xx} - s\widehat{\Delta t}\gamma'_{xx} - \gamma^* \tag{133}$$

$$= -\frac{2}{3}\hat{s}\Delta t^{1/2}\gamma_{xx} - \frac{2}{3}\hat{s}\Delta t^{1/2}\gamma'_{xx} + \frac{2}{3}\Delta t\gamma_t + O(\Delta t^3) \tag{134}$$

$$= \frac{4}{9}\hat{s}^2\Delta t\gamma_{xxxx} - \frac{2}{3}\Delta t M\lambda\gamma_{xx}F''(\gamma) - \frac{2}{3}\Delta t M\lambda\gamma_x\gamma_x F'''(\gamma) + \frac{2}{3}\Delta t\gamma_t - \frac{4}{3}\hat{s}\Delta t^{5/2}\gamma_{ttxx} + O(\Delta t^3) \tag{135}$$

$$= \frac{2}{3}\Delta t\left(\gamma_t - M\lambda(F'(\gamma) - \gamma_{xx})_{xx}\right) - \frac{4}{3}\hat{s}\Delta t^{5/2}\gamma_{ttxx} + O(\Delta t^3) \tag{136}$$

$$= -\frac{4}{3}\hat{s}\Delta t^{5/2}\gamma_{ttxx} + O(\Delta t^3) \tag{137}$$

Thus we see an $O(\Delta t^{5/2})$ local truncation error, which corresponds to a global truncation error of $O(\Delta t^{3/2})$, so that the discretization is formally order 1.5 accurate.

5. Numerical examples

All the units in the following tests are SI units.

5.1. Manufactured solution

In this test, we evaluate the accuracy of our discrete solvers using a manufactured solution for γ and $\mathbf{u}$. We choose the source terms to enforce the manufactured solution as

$$S_\gamma = \frac{\partial\gamma}{\partial t} + \nabla\cdot(\mathbf{u}\gamma) - \nabla\cdot(M\nabla\xi) \tag{138}$$

$$S_{\mathbf{u}} = \frac{\partial\rho\mathbf{u}}{\partial t} + \nabla\cdot(\mathbf{m}\otimes\mathbf{u}) + \nabla p - \rho g - \sigma\kappa\nabla(g(\gamma)) - \nabla\cdot\left(\mu\left(\nabla\mathbf{u} + (\nabla\mathbf{u})^T\right)\right). \tag{139}$$

We compute the error and its order at the end of the simulation to measure the accuracy of our method. We first assess the accuracy of the Cahn-Hilliard solver alone. We then incorporate the Navier-Stokes solve and evaluate the accuracy of the full method. Our parameters are chosen following [31]. In this section, we use a square domain $[-\pi,\pi]^2$. We set the density of the fluid phases to be $\rho_0 = 1$ and $\rho_1 = 3$, with viscosities $\mu_0 = 0.01$ and $\mu_1 = 0.02$. We use a time step of $\Delta t = 0.08/N$ and cell size $\Delta x = 2\pi/N$. We select the Cahn-Hilliard parameters M, σ, and η such that $M = 0.001$, $\lambda = 0.001$, and $\eta = 0.1$.

Table 1: Analysis of our Cahn-Hilliard solver at $t = 1$ demonstrates second order convergence.

	γ			
N	L_2		L_∞	
8	1.79e-05		2.96e-05	
16	4.40e-06	2.03	7.73e-06	1.93
32	1.23e-06	1.84	2.04e-06	1.92
64	3.03e-07	2.02	5.32e-07	1.94
128	7.65e-08	1.99	1.39e-07	1.93
256	1.98e-08	1.95	3.71e-08	1.91

Table 2: Analysis of our Cahn-Hilliard-Navier-Stokes solver at $t = 1$ demonstrates second order convergence.

	γ				u				v				p			
N	L_2		L_∞		L_2		L_∞		L_2		L_∞		L_2		L_∞	
8	1.86e-02		3.24e-02		6.88e-02		1.69e-01		1.40e-02		3.60e-02		1.60e-02		4.38e-02	
16	3.33e-03	2.48	1.20e-02	1.44	1.42e-02	2.28	4.12e-02	2.04	3.17e-03	2.14	9.93e-03	1.86	3.45e-03	2.21	1.31e-02	1.74
32	5.74e-04	2.54	2.43e-03	2.30	3.40e-03	2.06	1.01e-02	2.04	7.43e-04	2.09	3.05e-03	1.70	7.92e-04	2.12	3.64e-03	1.85
64	1.10e-04	2.38	2.80e-04	3.12	8.53e-04	1.99	2.54e-03	1.98	1.83e-04	2.02	7.22e-04	2.08	1.89e-04	2.07	6.32e-04	2.52
128	2.75e-05	2.00	7.30e-05	1.94	2.16e-04	1.98	6.14e-04	2.05	4.60e-05	1.99	1.83e-04	1.98	4.85e-05	1.96	1.39e-04	2.19
256	6.85e-06	2.01	1.90e-05	1.94	5.62e-05	1.94	1.40e-04	2.13	1.25e-05	1.88	4.80e-05	1.93	1.35e-05	1.84	3.76e-05	1.89

5.1.1. Cahn-Hilliard solver

We assess the convergence of our Cahn-Hilliard discretization using the manufactured solution

$$\gamma(x, y, t) = \frac{1}{2}(\cos(x)\cos(y) + 1)\sin(t). \tag{140}$$

To focus solely on the accuracy of the Cahn-Hilliard discretization, we exclude the Navier-Stokes update and set $u = v = 0$. We set the initial and boundary conditions using the manufactured solution. We measure the error in our simulation at $t = 1$. We determine the L_2 and L_∞ convergence by refining N from 8 to 256 with a constant $\frac{\Delta t}{\Delta x}$. The results are listed in Table 1 and show that our Cahn-Hilliard discretization is second order accurate.

5.1.2. Cahn-Hilliard-Navier-Stokes solver

We evaluate the convergence of our full method employing both the Cahn-Hilliard and Navier-Stokes solves. For this purpose, we utilize the following manufactured solutions for γ, $\mathbf{u}$, and p, which we have adapted from the corresponding solution in [31]:

$$\gamma(x, y, t) = \frac{1}{2}(\cos(x)\cos(y) + 1)\sin(t) \tag{141}$$

$$u(x, y, t) = \sin(x)\cos(y)\cos(t) \tag{142}$$

$$v(x, y, t) = -\cos(x)\sin(y)\cos(t) \tag{143}$$

$$p(x, y, t) = \cos(x)\cos(y)\sin(t) \tag{144}$$

Note that these continuous solutions maintain a divergence-free velocity field, $\nabla \cdot \mathbf{u} = 0$. Additionally, gravity is $g = (1, -2)$. We set the initial and boundary conditions using the manufactured solution. We measure the error for γ, $\mathbf{u}$, and p at $t = 1$. We determine the L_2 and L_∞ convergence by refining N from 8 to 256 with a constant $\frac{\Delta t}{\Delta x}$. As shown in Table 2, our method exhibits second-order accuracy in γ, $\mathbf{u}$, and p.

5.2. Binary separation of phases

In this test, we demonstrate the evolution of the fluid phase separation over time with $\mathbf{u} = 0$ and $S_\gamma = 0$ using a random initial distribution for γ. We use the same setup as in [28]. In the following tests, we use a square domain $[0, 2\pi]^2$ that is periodic in all directions. γ is randomly distributed uniformly in the range $[0.475, 0.575]$. We use a time step of $\Delta t = 0.0001$ and cell size $\Delta x = 1/512$, and we run the test to $t = 5$. We select the Cahn-Hilliard parameters M, σ, and η such that $ML = \eta^2$, $\sigma = 1$, and $\eta^2 = 0.001$.

Figure 5 shows the increasing phase separation from $t = 0$ to $t = 5$. Our results are qualitatively similar to the results depicted in [28].

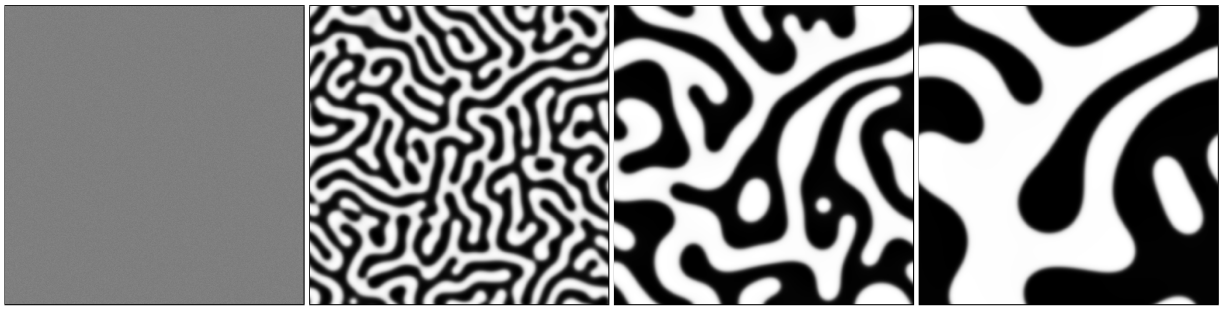

(a) $t = 0$ (b) $t = 0.1$ (c) $t = 1$ (d) $t = 5$

Fig. 5: Binary fluid separation over time

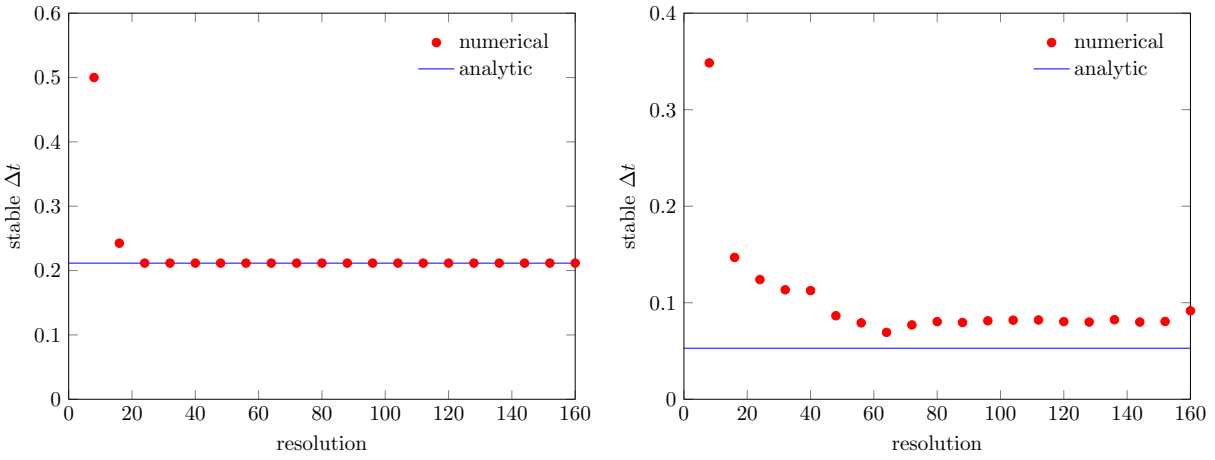

Fig. 6: Numerically determined stable time step size compared with the analytically predicted for (left) linearized problem and (right) the fully nonlinear problem. The stable time step size does not depend significantly on resolution and is in close agreement with the analytical prediction.

5.3. Discretization stability

In this test, we numerically evaluate the stability of our Cahn-Hilliard discretization and verify the analytical stability analysis we performed in Section 4.1. The first test we perform is to mimic the stability analysis setup, where we run Cahn-Hilliard without advection ($\mathbf{u} = 0$) using a linearized chemical potential derivative $F'(\gamma) = \frac{\gamma}{\eta^2}$, which mimics the scaling on the nonlinear potential. We use $[0, 1]^2$ with periodic boundary conditions as our domain, and we fix $\eta = 0.01$, $M = 0.001$, and $\lambda = 0.001$. We do not perform the postprocessing step to keep γ in bounds. γ is initialized randomly between 0 and 1. If stable, this simulation will converge to a constant γ, whose value is equal to the average of the original values, which will be close to 0.5. If unstable, the simulation diverges. For the purposes of this test, we define a simulation to be unstable if during the first 10^4 time steps $\gamma \geq 2$ is observed. For each $\Delta x = \frac{1}{N}$ with $N = 8, 16, 24, \ldots, 160$ we numerically search for the maximum stable time step size Δt_s and minimum unstable time step size Δt_u using binary search, stopping when $\Delta t_u - \Delta t_s < 10^{-4}$. Noting that $k = \eta^{-2} = 10^4$, the predicted stable time step size from (118) is approximately 0.2115 with no dependence on Δx. Numerically we computed $\Delta t_s \approx 0.2116$ and $\Delta t_u \approx 0.2117$ at all resolutions $N \geq 24$ and higher values for $N = 8, 16$. The results are shown in Figure 6. The numerically evaluated stable time step size is expected to be slightly larger that the analytical one, since there will be a range of time step sizes that are unstable but which take more than 10^4 time steps to diverge far enough to reach $\gamma = 2$.

We repeat the test with the same parameters and setup but using the original nonlinear chemical potential so that the system undergoes phase separation. We compute Δt_s and Δt_u as before. The results are shown in Figure 6. The stable time step stabilizes at $\Delta t_s \approx 0.07 - 0.08$ across resolutions, except for $N = 8 - 40$, where significantly larger time step sizes are stable. For the stable equilibria at $\gamma = 0$ and $\gamma = 1$ we have $k = F''(\gamma) = 2\eta^{-2}$, which corresponds to a stable time step size of 0.05288. We conclude from this that the linearized analysis provides a reasonable estimate of

Table 3: Material settings for different cases of the stationary circle test.

Case ID	ρ_0	ρ_1	μ_0	μ_1	σ
Case 1	1000	1000	0	0	1
Case 2	1000	1000	0.1	0.1	1
Case 3	1	1000	0.1	0.1	1
Case 4	1000	1000	0.0001	0.1	1
Case 5	1000	1000	0.1	0.1	10

the stability of the nonlinear Cahn-Hilliard discretization in the absence of advection. This is perhaps not surprising, since $\gamma \approx 0$ or $\gamma \approx 1$ most of the time. In particular, the insensitivity of Δt_s to Δx is also observed in the nonlinear case.

5.4. Stationary circle

We simulate a stationary drop with zero initial velocity and pressure using the same parameters as [31]. In an ideal system, the pressure and surface tension forces balance, and therefore the drop should maintain its shape and remain stationary. Discretely solving the system introduces spurious currents, leading to deformation. This test quantifies these currents and observes the impact of altering the resolution, density ratio, viscosity, and surface tension. The test is carried out in a $[0, 1]^2$ domain and time step of $\Delta t = 0.064/N$ and cell size $\Delta x = 1/N$. All walls are modeled with free-slip boundary conditions. The simulation runs until $t = 10$.

The initial configuration features a drop with initial radius of $r = 0.2$, centered at $(0.5, 0.5)$. The drop, designated as fluid 1, has a density of $\rho_1 = 1000$ and a viscosity that varies according to test case. The density and viscosity of the fluid surrounding the drop vary in each case. The specific values are detailed in Table 3 for density, viscosity and surface tension. Cases 2 and 4 investigate the effect of viscosity, while case 3 examines the impact of viscosity with a larger density ratio. Lastly, case 5 investigates the effects of surface tension.

We set $\eta = \eta_0(\Delta x/h_0)^{X^\eta} = \eta_0(Nh_0)^{-X^\eta}$ and $M = M_0(\eta/\eta_0)^{X^M} = \frac{M_0}{Nh_0}$ where $\eta_0 = h_0 = 1/32$, $M_0 = 10^{-5}$, $X^\eta = 2/3$ and $X^M = 3/2$. Note that we choose a larger value for M than what was used in [31] since we observed their M to be insufficient to maintain a steady interface using our method. We refine N from 16 to 256 and compute the L_2 and L_∞ errors by comparing the magnitude of velocity $\|\mathbf{u}\|_2$ averaged to each cell center with zero. The effect of refinement in each case is illustrated in Figure 7. We observe that refinement shows a decrease in the L_2 and L_∞ errors for most cases of slightly better than first order. However, in the case without viscosity, we note that the L_∞ error does not show much decrease with refinement.

The above test couples the parameters η and M to the refinement parameter N to test convergence to the sharp interface solution. This means that the coefficients of the PDE are changing under refinement, and therefore the test is not a proper convergence test. As further examination of the convergence properties of the proposed method on this test, we repeat the test with the PDE fixed for a proper refinement study. The results with fixed parameters $\eta = 0.02$ and $M = 10^{-6}$ are shown in Figure 8. We observe convergence closer to second order in both L_2 and L_∞ in this revised test and can conclude that while the method is somewhat sensitive to the sharpness of the interface, it does converge under refinement.

5.5. Horizontal shear

The purpose of this test is to assess the conservation of mass, momentum, and kinetic energy within our method. We evaluate several scenarios with different densities and viscosities in the absence of external forces. We replicate the test outlined in [31]. The domain is $[0, 1]^2$, with periodic boundary conditions on all sides. The cell size is $\Delta x = 1/128$. The initial velocity and γ are given by

$$u(x, y, 0) = \begin{cases} \tanh\left(\frac{y-y_1}{\delta_1}\right), & \text{if } y \le y_0 \\ \tanh\left(\frac{y_2-y}{\delta_1}\right), & \text{if } y > y_0 \end{cases} \tag{145}$$

$$v(x, y, 0) = \delta_2 \sin(kx) \tag{146}$$

$$\gamma(x, y, 0) = \begin{cases} \frac{1}{2}\left(1 + \tanh\left(\frac{y-y_1}{\delta_1}\right)\right), & \text{if } y \le y_0 \\ \frac{1}{2}\left(1 + \tanh\left(\frac{y_2-y}{\delta_1}\right)\right), & \text{if } y > y_0 \end{cases} \tag{147}$$

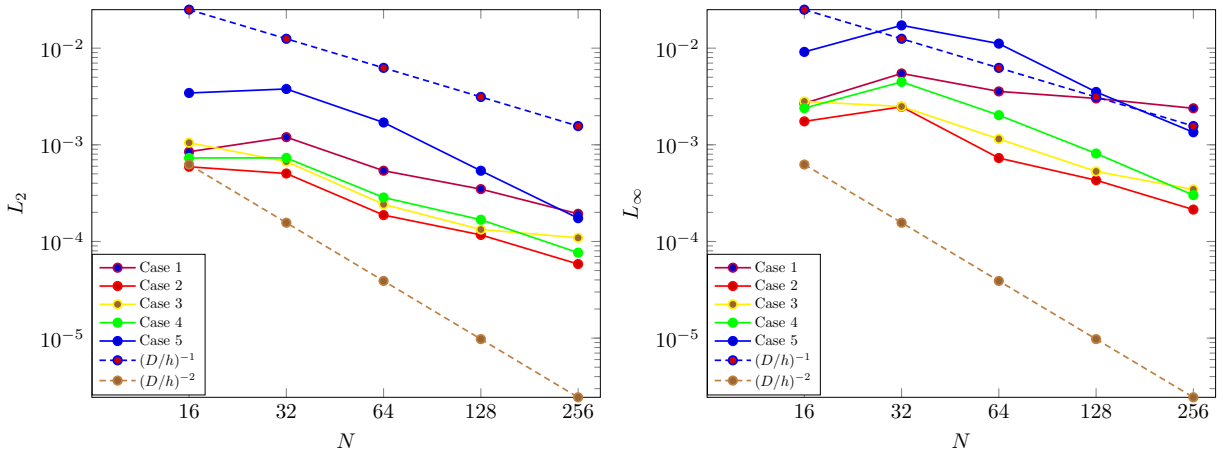

(a) L_2 error (b) L_∞ error

Fig. 7: L_2 and L_∞ errors of velocity in the stationary circle test.

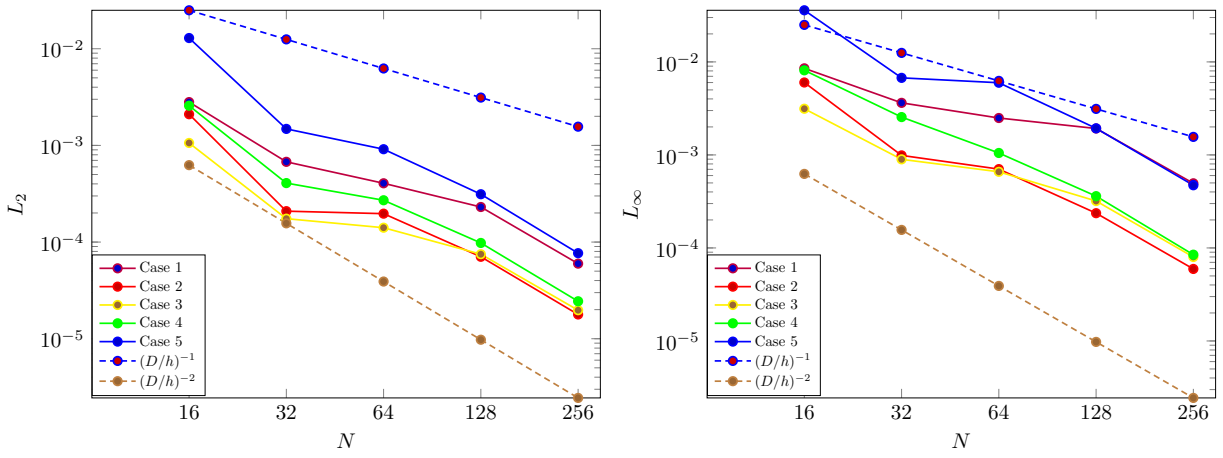

(a) L_2 error (b) L_∞ error

Fig. 8: L_2 and L_∞ errors of velocity in the stationary circle test with fixed interface width.

with $y_0 = 0.5, y_1 = 0.25, y_2 = 0.75, \delta_1 = 1/30, \delta_2 = 0.5$ and $k = 2\pi$. As shown in Figure 9, fluid 1 is initialized in a band at the center of the domain with a velocity with positive x component, and fluid 0 is initialized elsewhere with a velocity with negative x component, leading to a strong velocity gradient at the interface. We test four different cases, as described in Table 4. In all cases, the surface tension is set to $\sigma = 10^{-12}$. We vary density and viscosity across the four cases. The time step is $\Delta t = 0.0005$ and the simulation ends at $t = 1$. We set $\eta = \delta_1/\sqrt{2}$ and $M = 10^{-7}$.

Mass and momentum should be conserved in all four cases investigated. Since surface tension is negligible, kinetic energy should be conserved in inviscid cases and gradually decline in viscous cases. We calculate the total mass, momentum and kinetic energy as

$$m_{\text{total}} = \sum_{i,j} \left(\rho_0 + (\rho_1 - \rho_0)\,\gamma_{i,j}\right) \Delta\Omega \tag{148}$$

$$(m\mathbf{u})^x_{\text{total}} = \sum_{i,j} \left(\rho_{i-1/2,j}\right)\left(u_{i-1/2,j}\right) \Delta\Omega \tag{149}$$

$$E_k = \frac{1}{2} \sum_{i,j} \left(\left(\rho_{i-1/2,j}\right)\left(u_{i-1/2,j}\right)^2 + \left(\rho_{i,j-1/2}\right)\left(v_{i,j-1/2}\right)^2\right) \Delta\Omega, \tag{150}$$

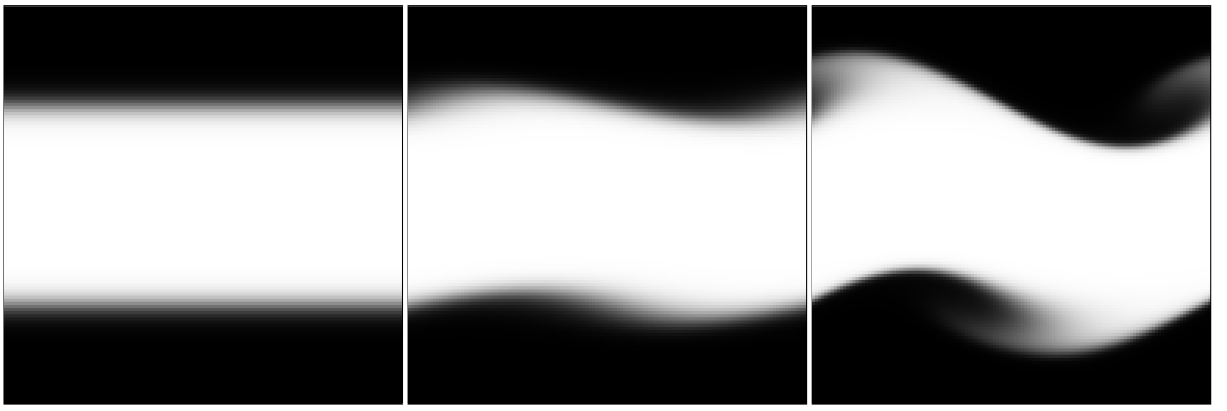

(a) $t = 0$ (b) $t = 0.5$ (c) $t = 1$

Fig. 9: Horizontal Shear (Case 3).

where $\Delta\Omega = \Delta x \Delta y$ is the cell volume, and $(m\mathbf{u})^y_{\text{total}}$ is computed analogously.

The results of the tests are presented in Figure 10. Cases 1 and 3 exhibits zero mass change, while cases 2 and 4 have small decline with a magnitude of 10^{-12}. As expected, the inviscid cases maintain constant kinetic energy, while cases 3 and 4, with viscosity, show a gradual decline. Because our velocities are stored on faces instead of cell centers, we compute our kinetic energy differently from [31], but we observe similar results. We observe almost no change in momentum for cases without viscosity, and we see a minor change in viscous cases.

5.5.1. Shearing artifacts with large gradients

We observe some artifacts at the interface at the tested resolutions for inviscid cases 1 and 2, as illustrated in Figure 11. Increasing the resolution from 128 to 512 demonstrates that the artifacts go away under refinement. The artifact is caused by consistent advection in the presence of sharp γ gradients and shearing flow. The artifact is not present if WENO advection is used for momentum advection, however that scheme fails to preserve numerical consistency of mass and momentum. Strengthening the effects of Cahn-Hilliard also eliminates the artifact. It is unknown if these artifacts were also present in [31], as they only give bulk averaged measurements (which are consistent with ours), which do not reveal the artifacts we observed.

5.6. Translating circle

This test examines the accuracy of advection in our method at different density ratios, based on the method used in [31]. We use a $[0, 1]^2$ domain, with a cell size of $\Delta x = 1/128$ and the time step of $\Delta t = \Delta x/10$, with periodic boundary conditions in all axes. The initial configuration of the test comprises a circular drop of fluid 1 with a radius of $r = 0.1$ centered at $(0.5, 0.5)$. The initial velocity is $\langle 1, 1 \rangle$ everywhere. The simulation ends at $t = 1$, when the drop is expected to return to the initial position. Fluid 1 is tested with varying densities of $\rho_1 = 1, 10^3, 10^6, 10^9$. The surrounding fluid 0 has density $\rho_0 = 1$. The viscosity of both fluids is zero. All density ratios are tested with surface tension values set to $\sigma = 1$ and $\sigma = 10^{-12}$. The test is carried out in the absence of external forces. We set $\eta = 3\Delta x$ and $M = 10^{-7}$. The material settings are summarized in Table 5.

In the ideal solution of the test, the drop returns to its initial location, preserving its original circular shape. The velocity remains constant throughout the simulation for all cases. Pressure maintains its initial value of zero in the absence of surface tension. However, in the presence of surface tension, a pressure jump should be observed around

Table 4: Material settings for different cases of the horizontal shear.

Case ID	ρ_0	ρ_1	μ_0	μ_1
Case 1	1	1	0	0
Case 2	1	10	0	0
Case 3	1	1	0.001	0.01
Case 4	1	10	0.001	0.01

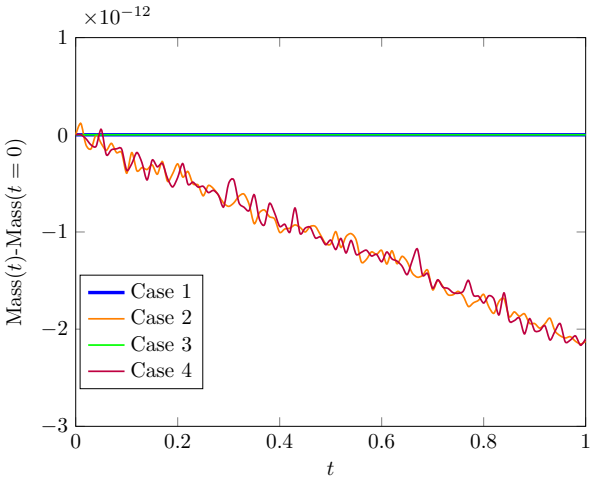

(a) Change in mass over time.

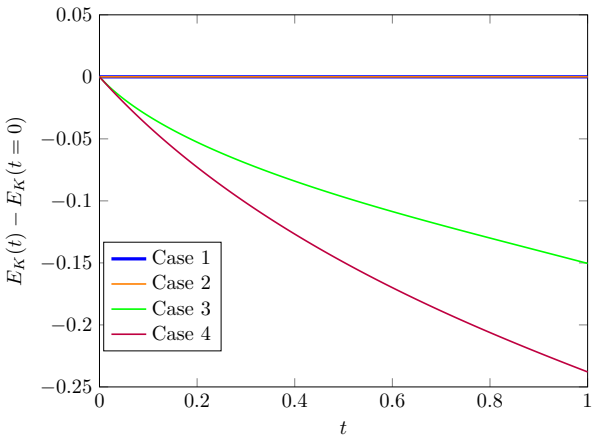

(b) Change in Kinetic Energy over time.

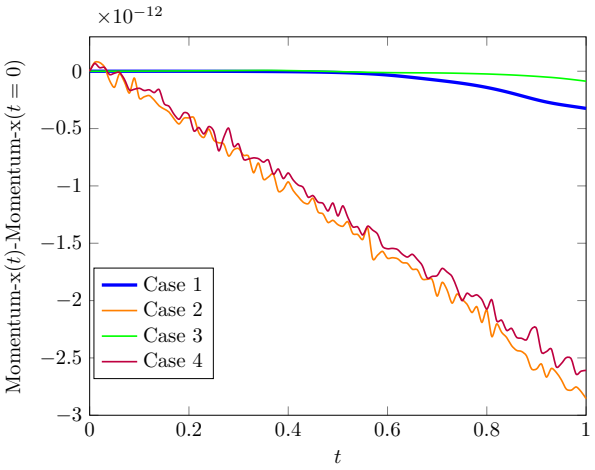

(c) Change in momentum (x axis).

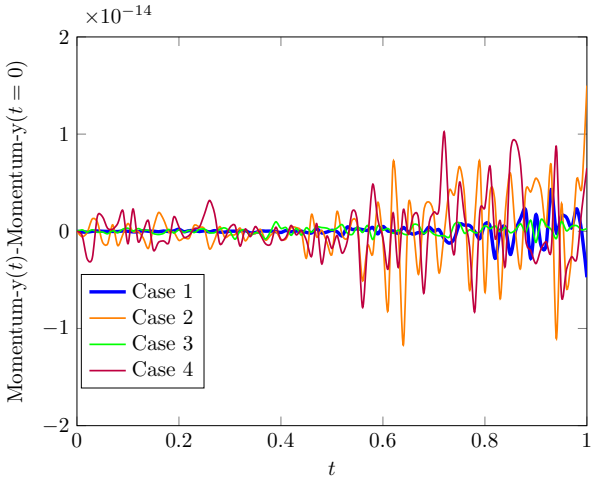

(d) Change in momentum (y axis).

Fig. 10: Results of the horizontal shear test for Cases 1-4.

the surface of the bubble. A snapshot of velocity streamlines at the conclusion of the simulation is depicted for cases without surface tension in Figure 12, and with surface tension in Figure 13 . The drop consistently preserves its shape until the end of the simulation, and velocities remain almost constant, aligning with their initial streamlines in both cases.

The L_2 and L_∞ errors for velocities are detailed in Tables 6 and 7 for cases without and with surface tension, respectively. The error is computed by comparing the final velocities with the initial value. We observe that our error is inversely correlated with the density ratio in cases without surface tension and they are consistent with the findings reported by Huang et al. [31], and the errors in the cases with surface tension are somewhat better.

5.7. Rising air bubble

The primary objective of this experiment is to assess the convergence of our method toward the sharp interface solution within a real-world scenario characterized by a substantial difference in density and viscosity. This evaluation holds particular significance because it examines the convergence toward the sharp interface solution by adjusting the parameter η while simultaneously modifying the resolution N. As suggested by the findings of Huang et al. [31], increasing the resolution while keeping η constant leads to the experiment's results converging toward a solution with a transitional region of length $O(\eta)$. However, by decreasing η while simultaneously augmenting the resolution, we ensure the convergence toward the desired sharp interface solution.

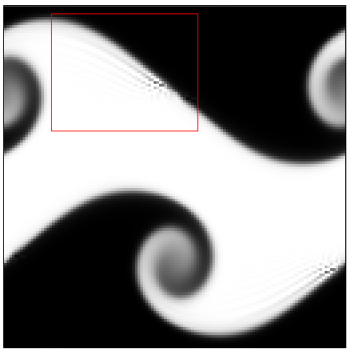

(a) One of the regions where artifacts can be seen in Case 1.

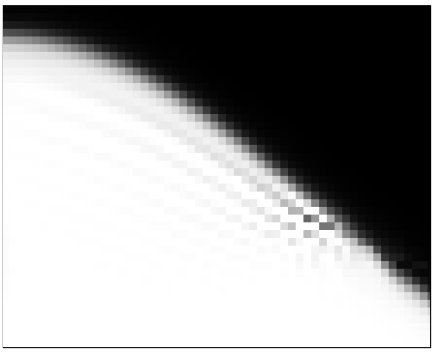

(b) A closer look at that region (a).

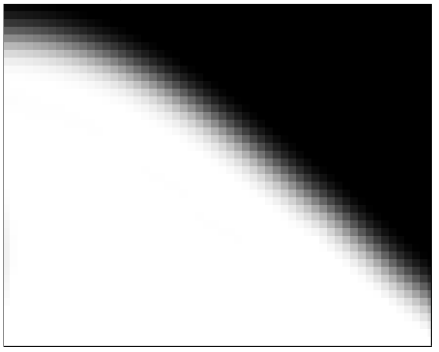

(c) The same region (a) if Case 1 is repeated with Cahn-Hilliard parameters $M = 10^{-5}$ and $\sigma = 1$ (no surface tension forces are applied in this example).

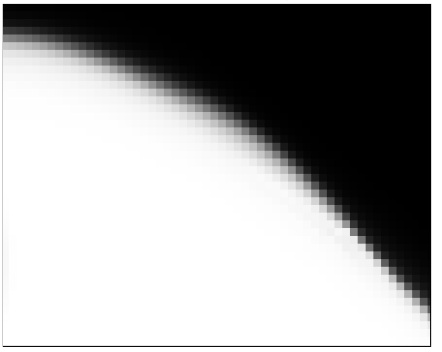

(d) The same region (a) if Case 1 is repeated using WENO advection for momentum advection.

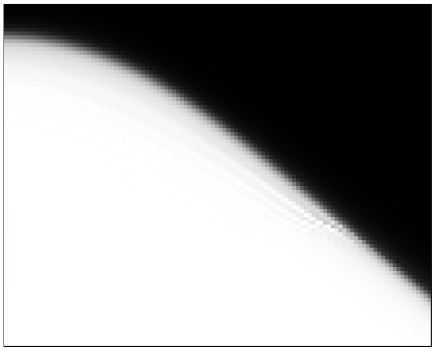

(e) The same region (a) if Case 1 is repeated with $N = 256$.

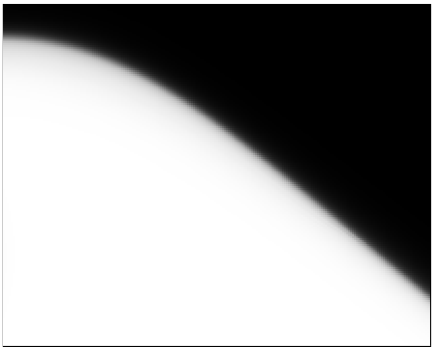

(f) The same region (a) if Case 1 is repeated with $N = 512$.

Fig. 11: Artifacts in horizontal shear Case 1, and the effects of different parameters and methods on those artifacts.

We examine a $[0, 1] \times [0, 2]$ domain with cell size $\Delta x = 1/N$. The top and bottom walls exhibit a no-slip boundary condition, while the left and right walls follow a slip boundary condition. The initial setup involves a bubble with an initial diameter of 0.5 positioned at the center $(0.5, 0.5)$ and assigned a zero initial velocity. Fluid 0 within the bubble has properties $\rho_0 = 1$ and $\mu_0 = 0.1$, whereas the surrounding fluid 1 has $\rho_1 = 1000$ and $\mu_1 = 10$. This results in a density ratio of 1000 and a viscosity ratio of 100. Surface tension σ is 1.96, and gravity is $(0, -0.98)$. The time step size is $\Delta t = 0.128/N$ and the simulation stops at $t = 1$. We reduce the length of the transition region by setting $\eta = \eta_0(Nh_0)^{-X_\eta}$ where $\eta_0 = h_0 = 1/32$. $X_\eta \leq 1$ so that we have the same number of cells in the transition region (or more) as we refine [31]. We set the mobility variable $M = M_0(\eta/\eta_0)^{X_M}$ where $M_0 = 10^{-7}$. Based on [32], X_M must be $1 \leq X_M < 2$.

We conduct six sets of tests and run each set with $N = 16, 32, 64, 128, 256$. In the first 5 sets of tests, we set $X_M = 1$ and $X_\eta = 0, \frac{1}{3}, \frac{1}{2}, \frac{2}{3}, 1$ to test the effects of X_η. In the last test, we set $X_M = \frac{3}{2}, X_\eta = \frac{2}{3}$ which makes $M \sim \Delta x$.

Table 5: Material settings for different cases of the translating circle test (surface tension, density).

Case ID	ρ_0	ρ_1	σ
Case 1	1	1	10^{-12}
Case 2	1	10^3	10^{-12}
Case 3	1	10^6	10^{-12}
Case 4	1	10^9	10^{-12}
Case 5	1	1	1
Case 6	1	10^3	1
Case 7	1	10^6	1
Case 8	1	10^9	1

Table 6: Error results for the advection test without surface tension.

Variable	Norm	$\rho_1/\rho_0 = 1$	$\rho_1/\rho_0 = 10^3$	$\rho_1/\rho_0 = 10^6$	$\rho_1/\rho_0 = 10^9$
u	L_2	8.81e-13	2.60e-13	3.49e-11	6.07e-08
	L_∞	7.36e-12	1.87e-12	2.55e-10	1.69e-06
v	L_2	8.81e-13	2.60e-13	3.49e-11	6.06e-08
	L_∞	7.36e-12	1.88e-12	2.55e-10	1.57e-06

Table 7: Error results for the advection test with surface tension.

Variable	Norm	$\rho_1/\rho_0 = 1$	$\rho_1/\rho_0 = 10^3$	$\rho_1/\rho_0 = 10^6$	$\rho_1/\rho_0 = 10^9$
u	L_2	7.93e-04	2.25e-05	7.44e-07	8.47e-08
	L_∞	6.42e-03	1.50e-04	5.40e-06	1.16e-06
v	L_2	7.93e-04	2.25e-05	7.44e-07	8.47e-08
	L_∞	6.42e-03	1.50e-04	5.40e-06	1.27e-06

To test the convergence of all test cases we compute the following three parameters:

$$\psi_c = \frac{P_a}{P_b} = \frac{2\sqrt{\int_{\gamma<\frac{1}{2}} \pi d\Omega}}{P_b} \tag{151}$$

$$y_c = \frac{\int_\Omega y(1-\gamma)d\Omega}{\int_\Omega (1-\gamma)d\Omega} \tag{152}$$

$$v_c = \frac{\int_\Omega v(1-\gamma)d\Omega}{\int_\Omega (1-\gamma)d\Omega}. \tag{153}$$

In (151), P_a is the perimeter of the circle with the same area as the bubble, P_b is the perimeter of the bubble and ψ_c is the circularity of the bubble. P_b is computed by discretizing the interface surface using a marching squares algorithm and computing the total length between successive nodes. $\psi_c = 1$ when the shape of the bubble is a circle and $\psi_c < 1$ when the bubble deforms [31]. y_c is center of mass and v_c is the velocity of center mass in the y direction (rising velocity).

In the case where $X_M = 1, X_\eta = 0$, we expect the simulation to converge to the exact solution of the phase-field model where $\eta = \eta_0$ since setting $X_\eta = 0$ results in using the same value for η in all of the simulations [31]. We show our results for this particular case in Figure 14. We observe that our results match the results shown in [31]. In the case where $X_\eta \neq 0$ we expect the simulation to converge to a sharp interface solution. We compare our results for each case where $N = 256$ in Figure 15. The error and convergence order of each case can be found in Table 8 where we compare all cases with $N = 16$ to $N = 128$ to the results from the simulation where $N = 256$. We observe second order convergence where $X_\eta = 0$ and maintain an order of about 1.5-2.0 on all other cases.

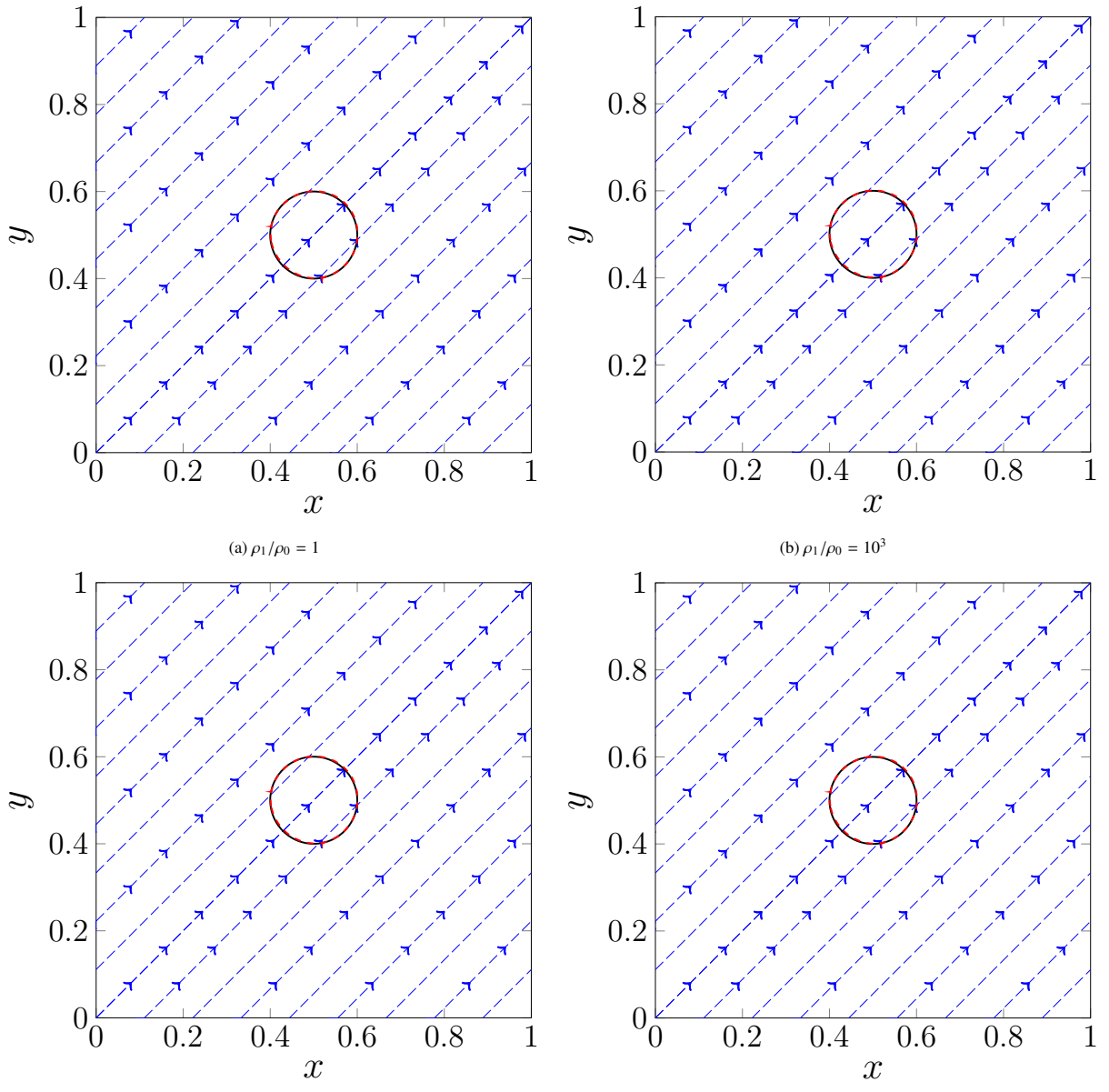

(a) $\rho_1/\rho_0 = 1$

(b) $\rho_1/\rho_0 = 10^3$

(c) $\rho_1/\rho_0 = 10^6$

(d) $\rho_1/\rho_0 = 10^9$

Fig. 12: Initial and final ($t = 1$) state of the drop with $\sigma = 10^{-12}$. The solid black line is the initial state and the dotted red line is the final state.

5.8. Comparisons of surface tension

The aim of this test is to compare different surface tension methods to determine how well they show expected properties. We measure the direction and location of surface tension in Section 5.8.1 and its effects on pressure in Section 5.8.2. We explore the impact of introducing $g(\gamma)$ as detailed in Section 3.2.3 and varying the parameter a in (47). The specific functions utilized in our comparative tests are outlined in Table 9. In cases 1 and 2 we use the surface tension used by Shen and Yang [51] and Huang et al. [31] respectively. Cases 3 to 7 we apply the function introduced in (47), varying the values of a as $a = 0, 0.1, 0.2, 0.3, 0.5$. In cases 8 and 9 we use the same scheme as cases 3 to 7 using a different functions as $g(\gamma)$. In all the tests described we set $\sigma = 1$.

We conduct the test in a $[0, 1]^2$ domain with a cell size of $\Delta x = 1/256$, where all the walls feature slip boundary conditions. We use $\Delta t = 0.00025$ and run the simulation until $t = 10$. The initial configuration features a bubble with an initial radius of $r = 0.2$, centered at $(0.5, 0.5)$, with zero initial velocity. The fluid inside the bubble and the

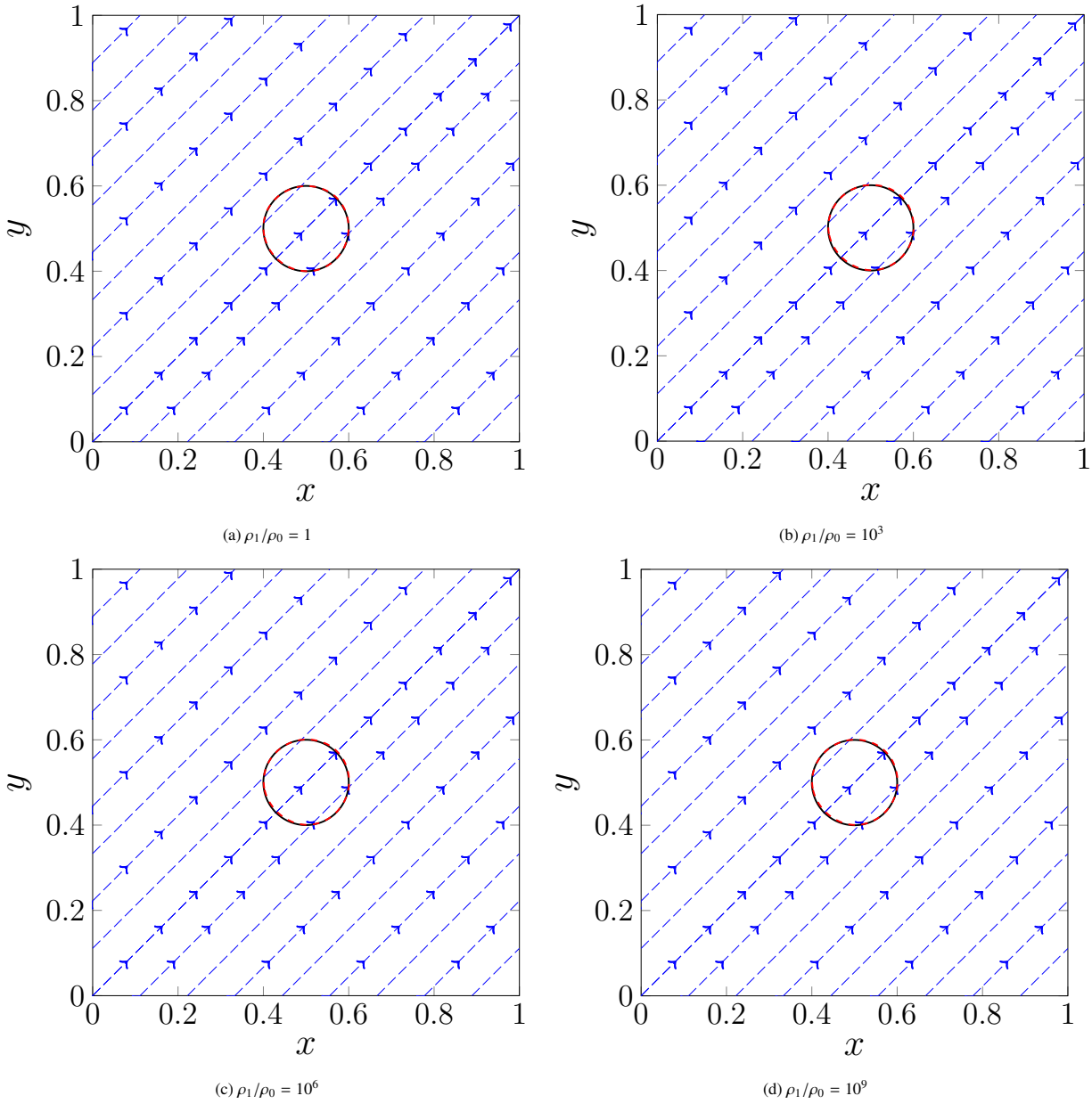

(a) $\rho_1/\rho_0 = 1$

(b) $\rho_1/\rho_0 = 10^3$

(c) $\rho_1/\rho_0 = 10^6$

(d) $\rho_1/\rho_0 = 10^9$

Fig. 13: Initial and final ($t = 1$) state of the drop with $\sigma = 1$. The solid black line is the initial state and the dotted red line is the final state.

surrounding fluid both have a density of $\rho_0 = \rho_1 = 1000$ and viscosity of $\mu_0 = \mu_1 = 0$.

We define η and M similar to Section 5.7, with $M_0 = 10^{-5}$, $\eta_0 = h_0 = 1/8$, $X^\eta = 2/3$ and $X^M = 3/2$. This gives $\eta = 0.03125$ and $M = 1.25 \times 10^{-6}$, which we use for all cases.

5.8.1. Magnitude and angle

Visual representations of the test results are shown in Figures 16 and 17. The angle between the surface normal and the surface tension force is measured in radians. The contour $\gamma = 0.5$ representing the center of the interface is displayed as a dashed circle.

Notably, cases 1 and 2 show strong disagreement between the surface tension direction and normal just beyond the interface center, and case 1 shows negligible magnitude at the interface center. Cases 2, 3, 8, and 9 all show strong disagreement in the angle far from the interface, but the magnitude of the surface tension in those areas is negligible

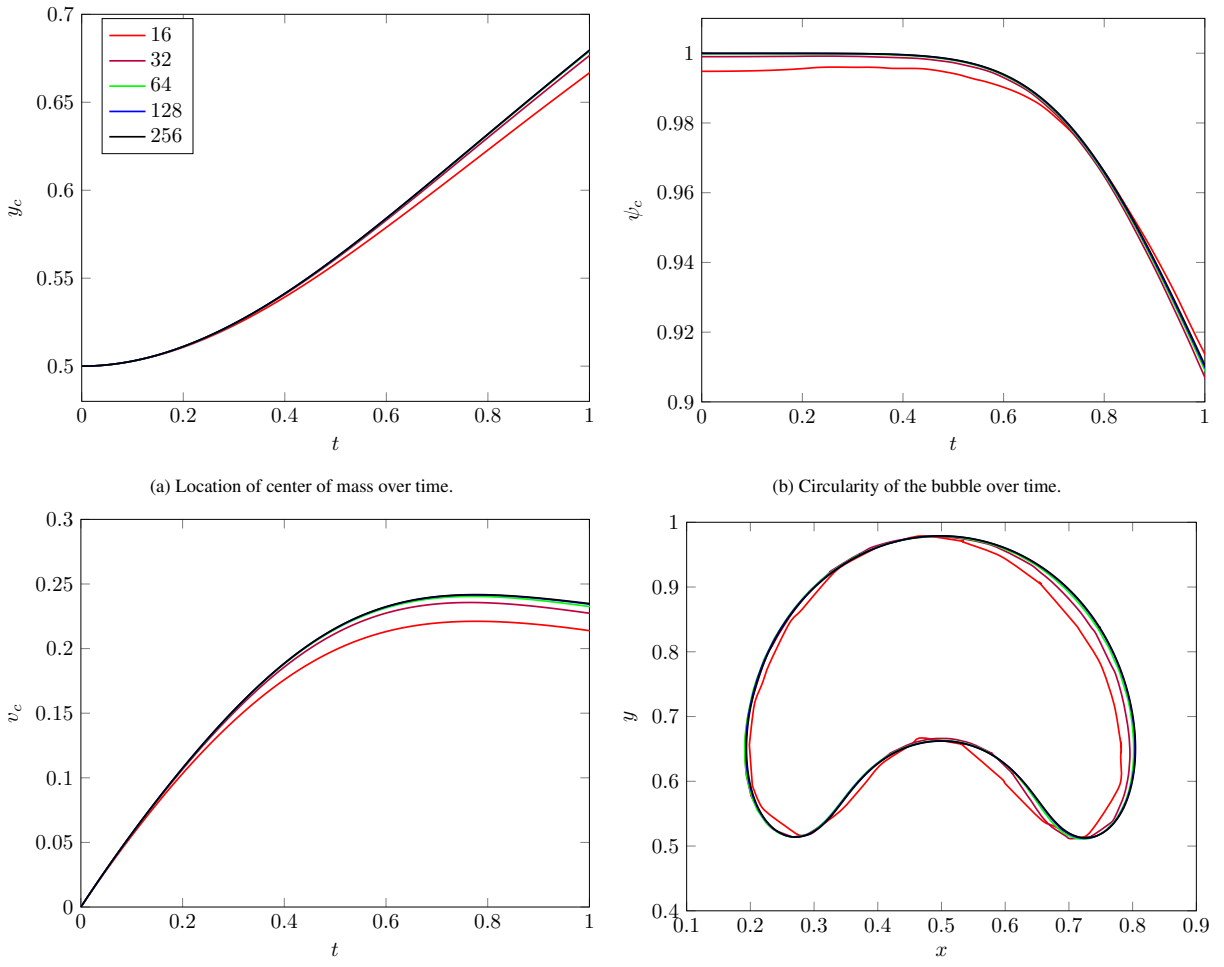

(a) Location of center of mass over time.

(b) Circularity of the bubble over time.

(c) Velocity of center of mass over time.

(d) Surface of the bubble at $t = 1$.

Fig. 14: Rising bubble test results with $X_\eta = 0, X_M = 1$.

as expected.

Cases 3 through 7 show the effects of the a parameter in our surface tension method. We observe that, as expected, the areas where the surface tension magnitude is nonzero begins to closely fit the interface center contour as a approaches 0.5. In the case where $a = 0.5$, the surface tension force closely matches the interface contour, as we would expect from a sharp interface solution. These cases also show the advantage of a finite support around the interface (in cases 4-7), which gives a surface tension force vector $\mathbf{0}$ away from the interface. In cases 3 (where $a = 0$), 8, and 9, we see that the surface tension is still being calculated away from the interface. While the magnitudes are negligible in these areas, they are not 0.

5.8.2. Effects on pressure

Ideally, we anticipate the pressure to be a constant value inside and outside of the bubble with a pressure jump on the surface. We compare our results to the ideal physical pressure along the x-axis at $y = 0.5$ in Figure 18.

We show in Figure 18a that as a goes from 0 to 0.5, the results move towards the ideal pressure jump caused by a sharp interface. All parameters of a produce acceptable results for pressure, which makes $\sigma\kappa\nabla g(\gamma)$ the best of the methods by this criteria. Figure 18b shows that cases 8 and 9, which are similar to our preferred method, are also reasonably close to the ideal pressure. Note that in Case 1, the formulation of the surface force introduces a gradient term which will be compensated for in the pressure correction; the plot for Case 1 shows the pseudo-pressure which includes the compensating term [53]. Case 2 deviates significantly (about 15%) from the ideal in our tests; this is

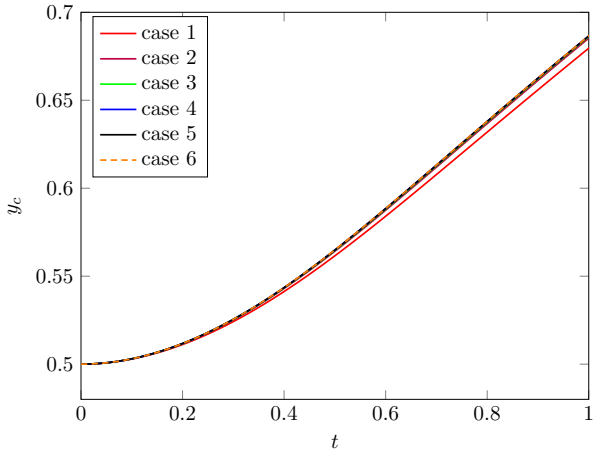

(a) Location of center of mass over time.

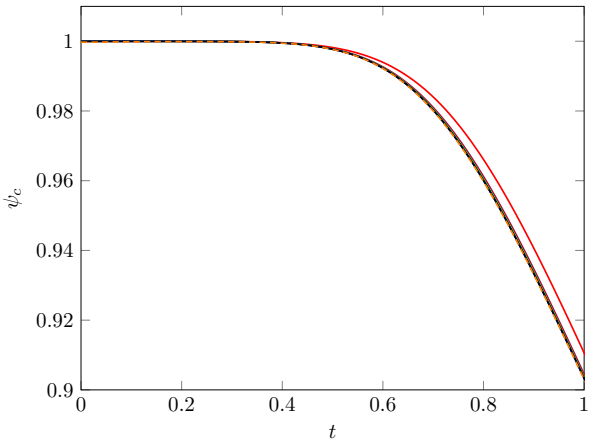

(b) Circularity of the bubble over time.

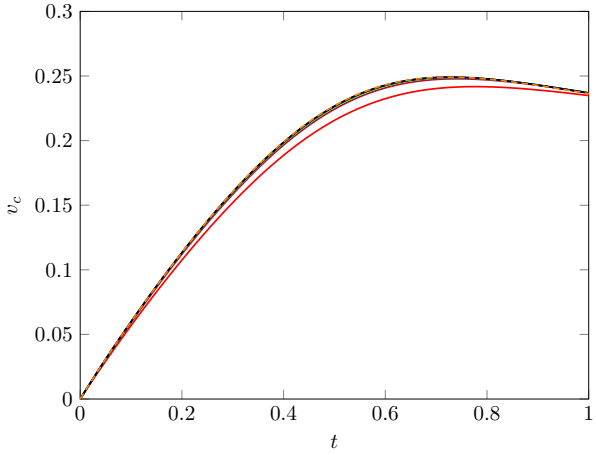

(c) Velocity of center of mass over time.

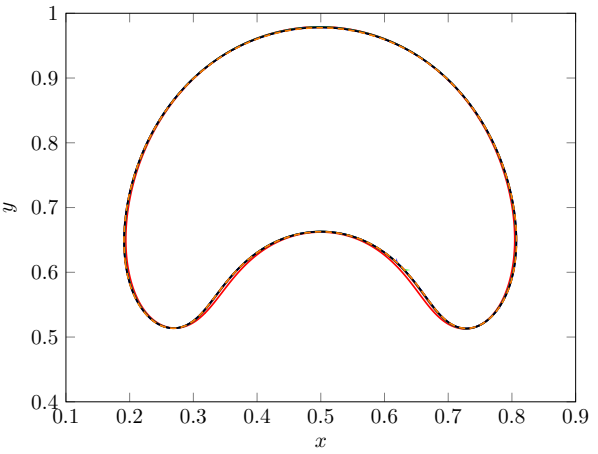

(d) Surface of the bubble at $t = 1$.

Fig. 15: Rising bubble test results of test described in table 8 with $N = 256$.

consistent with Huang et al. [31], which reported errors of about 9% on a similar test at lower resolution.

5.9. Rayleigh-Taylor instability

We simulate the classic Rayleigh-Taylor instability, where a denser fluid is initially positioned above a lighter one in the presence of gravitational force. This instability test serves as a benchmark for evaluating the behavior of two-phase flows. The tests was first investigated by Rayleigh [49] and is normally characterized by "Atwood ratio" $A_t = (\rho_1 - \rho_0)/(\rho_1 + \rho_0)$, a measure of the density difference between the two phases. Daly [11] conducted a numerical analysis of the test. Long-time instability analysis of the test for inviscid incompressible fluids without surface tension with $A_t = 0.5$ is done by Tryggvason [55]. We examine a $[0, 1] \times [0, 4]$ domain with cell sizes $\Delta x = 1/128$. Free-slip boundary conditions are enforced at the top and bottom walls, while the left and right walls are subject to periodic boundary conditions. The initial setup involves a heavier fluid with density $\rho_1 = 3, 30, 1000, 3000$ and viscosity $\mu_1 = 0.001$ positioned on top of a lighter fluid with density $\rho_0 = 1$ and viscosity $\mu_0 = 0.001$. The velocity is initialized to zero, and the initial interface between the two fluids is situated at $y = 2 + 0.1\cos(2\pi x)$. The specified parameters for the simulation include a surface tension $\sigma = 10^{-12}$, gravitational force vector $\langle 0, -1 \rangle$, and a time step size of $\Delta t = 5 \times 10^{-4}/\sqrt{A_t}$. The simulation concludes at $t\sqrt{A_t} = 8$. We set M so that $\lambda M = 10^{-15}$ and $\eta = 0.01$.

Snapshots of the test with $\rho_1 = 3$ are presented in Figure 19, offering a comparative analysis with the outcomes from our implementation of Huang et al. [31]'s method. Notably, our simulation closely aligns with the results obtained by Huang et al. [31]. Figure 20 provides a visual depiction of the Rayleigh-Taylor test's progression at

	Grid	$X_\eta = 0, X_M = 1$		$X_\eta = \frac{1}{3}, X_M = 1$		$X_\eta = \frac{1}{2}, X_M = 1$		$X_\eta = \frac{2}{3}, X_M = 1$		$X_\eta = \frac{2}{3}, X_M = \frac{3}{2}$		$X_\eta = 1, X_M = 1$	
		L_2		L_2		L_2		L_2		L_2		L_2	
ψ_c	16	3.54e-03		7.60e-03		9.70e-03		1.22e-02		1.21e-02		1.88e-02	
	32	2.50e-03	0.51	1.85e-03	2.04	2.26e-03	2.10	2.46e-03	2.30	2.45e-03	2.31	2.61e-03	2.85
	64	1.06e-03	1.24	8.01e-04	1.21	8.01e-04	2.10	9.07e-04	1.44	9.36e-04	1.39	1.20e-03	1.12
	128	3.92e-04	1.44	3.00e-04	1.42	2.58e-04	1.63	4.47e-04	1.02	4.86e-04	0.95	6.94e-04	0.80
		L_2		L_2		L_2		L_2		L_2		L_2	
y_c	16	9.24e-03		1.50e-02		1.69e-02		1.88e-02		1.87e-02		2.36e-02	
	32	2.27e-03	2.03	6.23e-03	1.27	6.86e-03	1.30	7.12e-03	1.40	7.10e-03	1.40	7.17e-03	1.72
	64	4.61e-04	2.30	2.65e-03	1.23	2.68e-03	1.30	2.47e-03	1.53	2.45e-03	1.53	1.92e-03	1.90
	128	6.49e-05	2.83	9.49e-04	1.48	8.64e-04	1.63	7.05e-04	1.81	6.96e-04	1.82	4.26e-04	2.17
		L_2		L_2		L_2		L_2		L_2		L_2	
v_c	16	1.75e-02		2.42e-02		2.65e-02		2.89e-02		2.89e-02		3.53e-02	
	32	5.71e-03	1.62	1.00e-02	1.27	1.07e-02	1.31	1.10e-02	1.40	1.10e-02	1.40	1.10e-02	1.68
	64	1.68e-03	1.76	4.06e-03	1.30	4.05e-03	1.31	3.75e-03	1.55	3.76e-03	1.55	2.99e-03	1.88
	128	3.00e-04	2.49	1.36e-03	1.58	1.25e-03	1.70	1.06e-03	1.82	1.07e-03	1.81	6.83e-04	2.13

Table 8: L_2 error and order compared to $N = 256$ on all the cases for rising air bubble test.

Table 9: Material settings for different cases for the surface tension and pressure comparison test.

Case ID	Surface Tension	a
Case 1	$\lambda\nabla\cdot(\nabla\gamma\otimes\nabla\gamma)$	
Case 2	$4\xi\nabla\gamma$	
Case 3	$\sigma\kappa\nabla(g(\gamma))$	0
Case 4	$\sigma\kappa\nabla(g(\gamma))$	0.1
Case 5	$\sigma\kappa\nabla(g(\gamma))$	0.2
Case 6	$\sigma\kappa\nabla(g(\gamma))$	0.3
Case 7	$\sigma\kappa\nabla(g(\gamma))$	0.5
Case 8	$\sigma\kappa\nabla\left(\frac{1}{2}\left(1+\tanh(4\gamma-2)\right)\right)$	
Case 9	$\sigma\kappa\nabla\gamma$	

a density ratio of 3, while Figure 21 showcases the evolution of simulations across various density ratios. In both Figure 20 and Figure 21, the simulations maintain symmetry throughout, even as the interface develops intricate shapes in later stages. As the density ratio increases, the simulation exhibits accelerated movement and a simpler evolution. Due to the minor impact of viscosity in these simulations, a stable state is not reached before the simulations conclude at $t\sqrt{A_t} = 8$.

In Figure 22 we plot a quantitative measurement of the test by measuring the highest and lowest point of the interface between the two fluids with density ratio of 3 from $t = 0$ to $t = 2.5$. Our results are comparable to the results reported by Huang et al. [31], [12] and Guermond and Quartapelle [20] which use similar values for density and viscosity.

5.10. Dam break

The dam break test is employed to assess the method's performance in scenarios characterized by high density ratios. In this test, we simulate the classic test as in Martin and Moyce [46] where a specific volume of water is confined within a rectangular box of dimensions $[a \times a]$, enclosed by walls on both the left and right sides. In the initial frame, the right wall of the box containing the water, is removed, leading to the observation of the gravitational evolution of water movement within a larger $[0, 4a] \times [0, 2a]$ domain. We examine this domain with cell sizes $\Delta x = a/64$ where $a = 0.05715$. The all the walls are subject to a no-slip boundary condition. The initial setup involves a heavier fluid (water) with density $\rho_0 = 998.207$ and viscosity $\mu_0 = 1.002 \times 10^{-3}$ confined in a $[a \times a]$ box surrounded by a lighter fluid (air) with density $\rho_1 = 1.204$ and viscosity $\mu_1 = 1.78 \times 10^{-5}$ with initial velocity of zero. The specified parameters for the simulation include a surface tension $\sigma = 7.28 \times 10^{-2}$, gravitational force vector $\langle 0, -9.8\rangle$, and a time step size of $\Delta t = 7.1437 \times 10^{-5}$. The simulation concludes at $t = 10$. We set M so that $\lambda M = 10^{-7}$ and $\eta = 0.01a$.

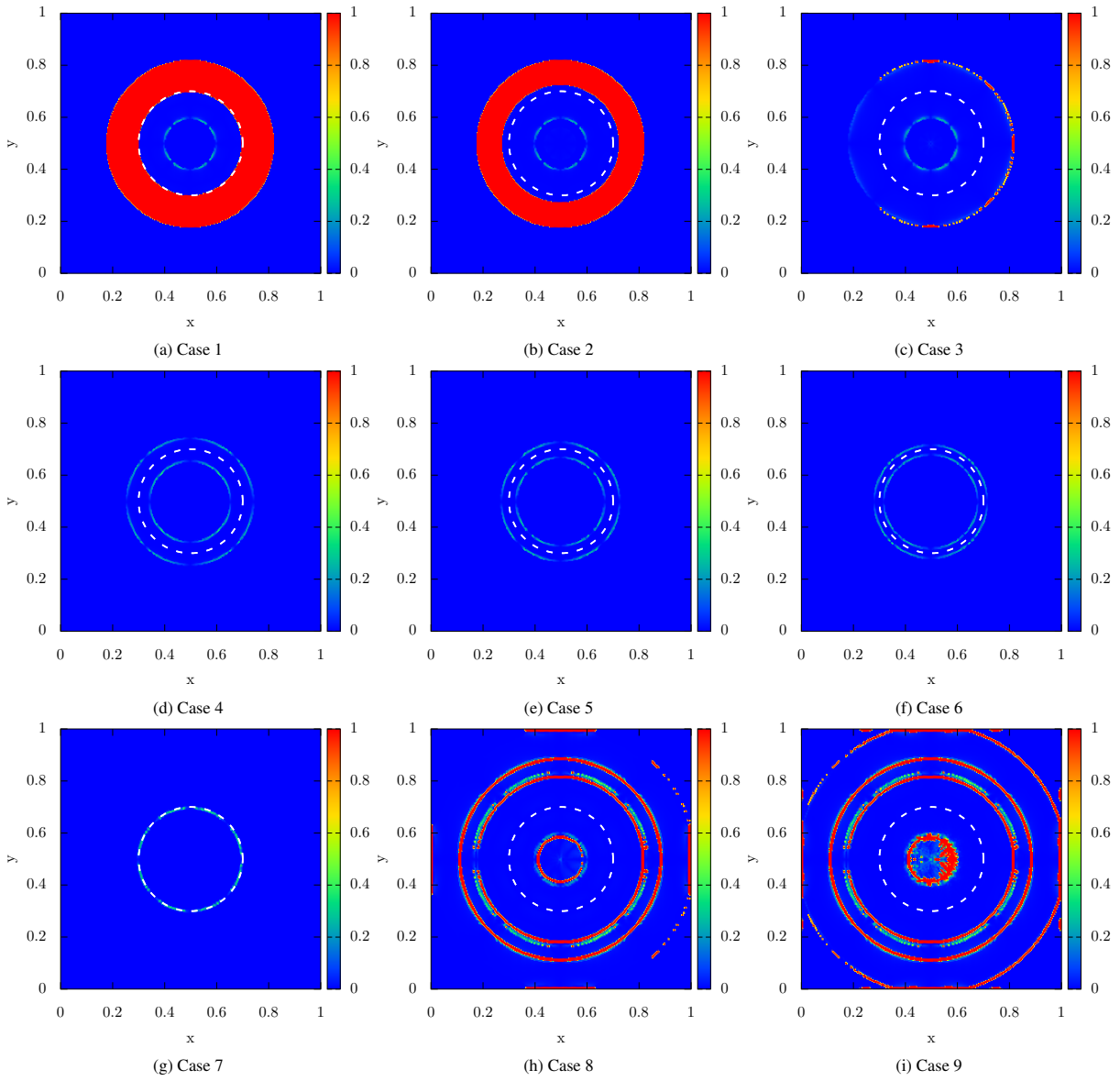

Fig. 16: Comparisons of the angle between surface tension force and surface normal (radians) for different surface tension formulations.

As previously noted, the simulation begins with zero velocity, and at time $t = 0$, removing the box containing the denser fluid instigates fluid motion due to gravity. As the simulation progresses, the denser fluid reaches the right wall of the domain, where it is pushed to rise along the wall before crashing back down. The simulation attains a stable condition by the conclusion of the simulation. Visual snapshots of distinct stages within the simulation are shown in Figures 24 and 25. We non-dimensionalize t by dividing it by $\sqrt{\frac{a}{|g_y|}}$ so that $T = t/\sqrt{\frac{a}{|g_y|}}$. We do the same for length as well by diving it by a. We measure our results quantitatively by computing the front of the interface and the highest point of the interface from $T = 0$ to $T = 2.5$ in Figure 23. Our results are comparable to those reported by Huang et al. [31] and Martin and Moyce [46].

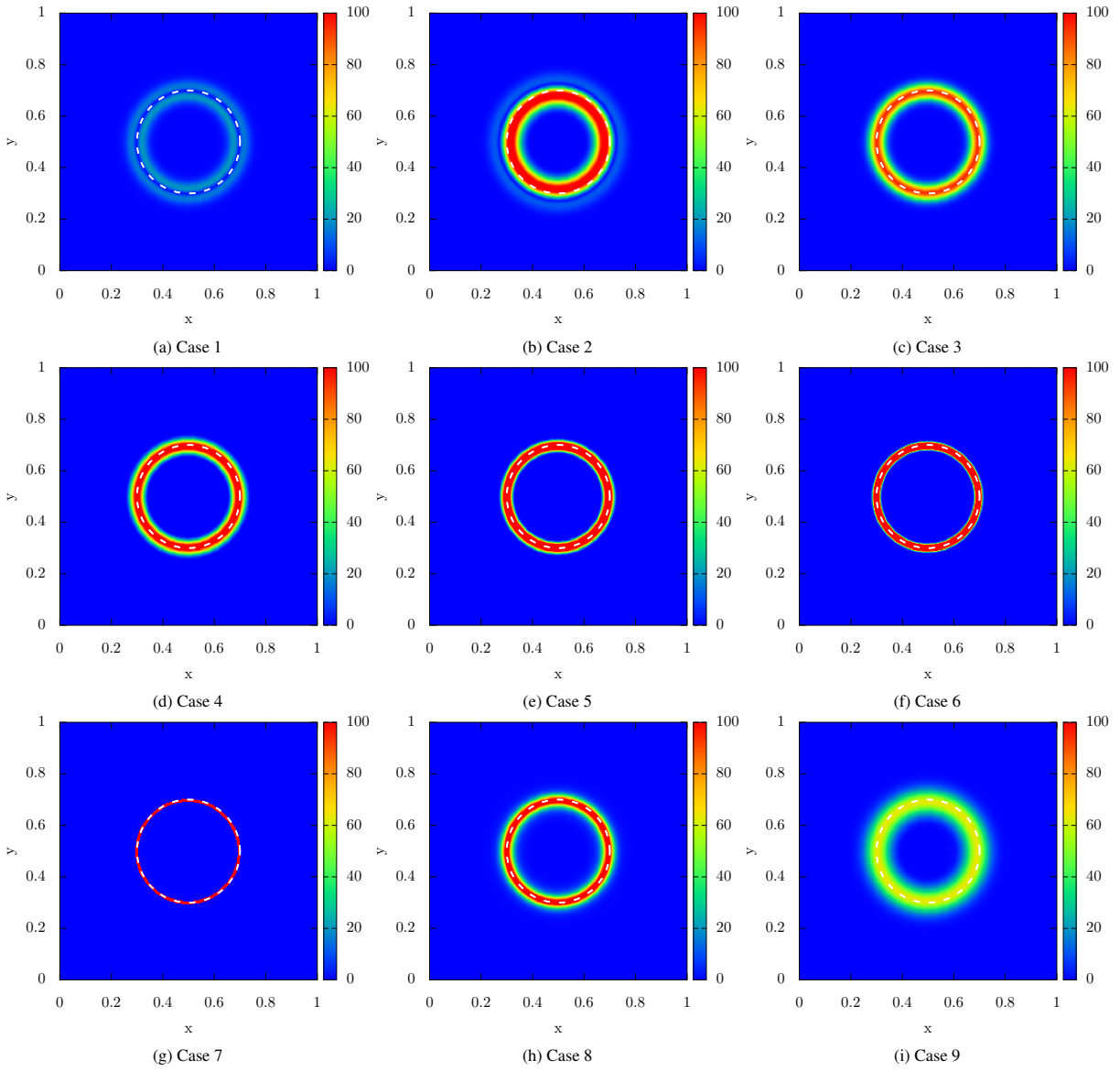

(a) Case 1 (b) Case 2 (c) Case 3

(d) Case 4 (e) Case 5 (f) Case 6

(g) Case 7 (h) Case 8 (i) Case 9

Fig. 17: Comparisons of the magnitude of surface tension force for different surface tension formulations.

5.11. Equilibrium Drop

We demonstrate the effects of setting boundary conditions for $\hat{\gamma}^{n+1}$ based on alternate contact angles. We adapt the Neumann boundary condition given in [31] as

$$\mathbf{n} \cdot \nabla \hat{\gamma}^{n+1} = \frac{\sigma}{2\lambda} \cos(\theta) \left(\frac{\pi}{2} \cos\left(\pi \gamma^{AB} - \frac{\pi}{2} \right) \right),$$

which allows for the choice of arbitrary interface-boundary contact angles. We follow the case setup used in [13, 31], where a drop of fluid with $r = 1$ is placed centered at the origin in a $[-3, 3] \times [0, 2]$ domain with cell size $\Delta x = 1/64$. No-slip boundary conditions are enforced at the top and bottom boundaries, and the left and right boundaries are periodic. The fluids have matched density $\rho_0 = \rho_1 = 1$ and viscosity $\mu_0 = \mu_1 = 1$, with surface tension $\sigma = 100$ and interface width $\eta = 0.02$. To match the non-dimensionalized Peclet number defined in [13], we set mobility $M = 1.885 \times 10^{-7}$. No gravity is used in this example. We run the simulation with time step size $\Delta t = 5 \times 10^{-5}$ and end at time $t = 1$.

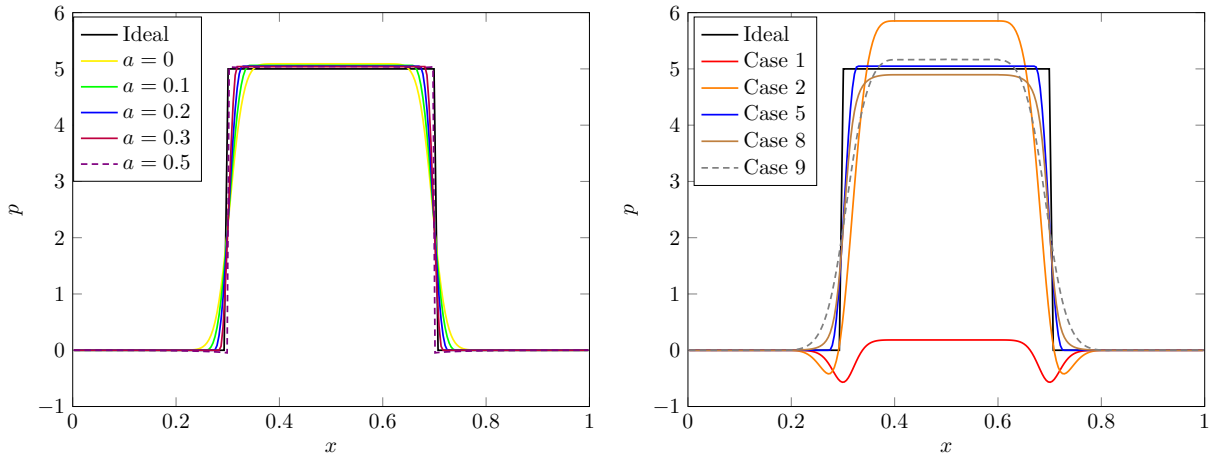

(a) Comparing pressure in cases using $\sigma\kappa\nabla(g(\gamma))$ for surface tension.

(b) Comparing pressure in the remaining cases with case 5 ($a = 0.2$).

Fig. 18: Change in pressure in the x axis at $y = 0.5$ of Section 5.8.

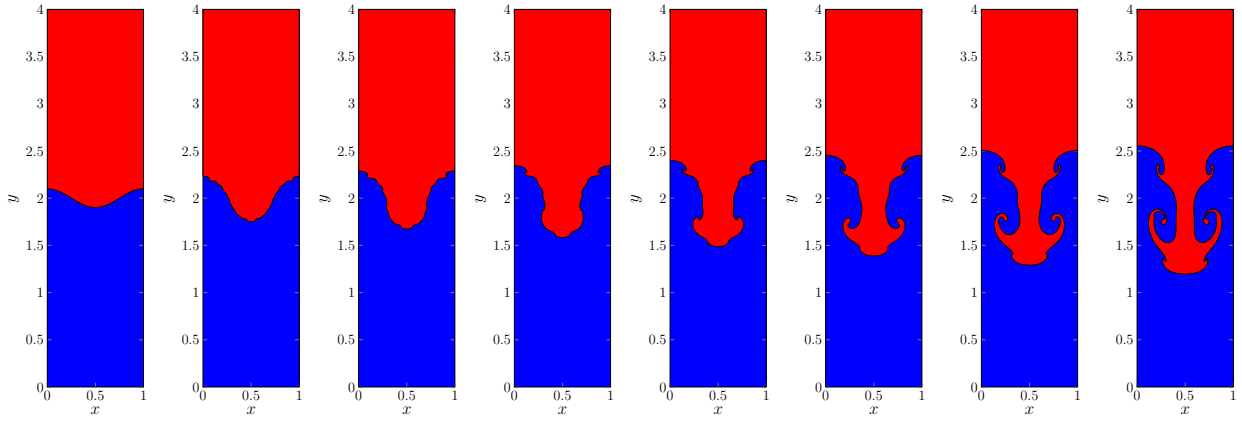

(a) Rayleigh-Taylor test results using Huang et al. [31]'s method.

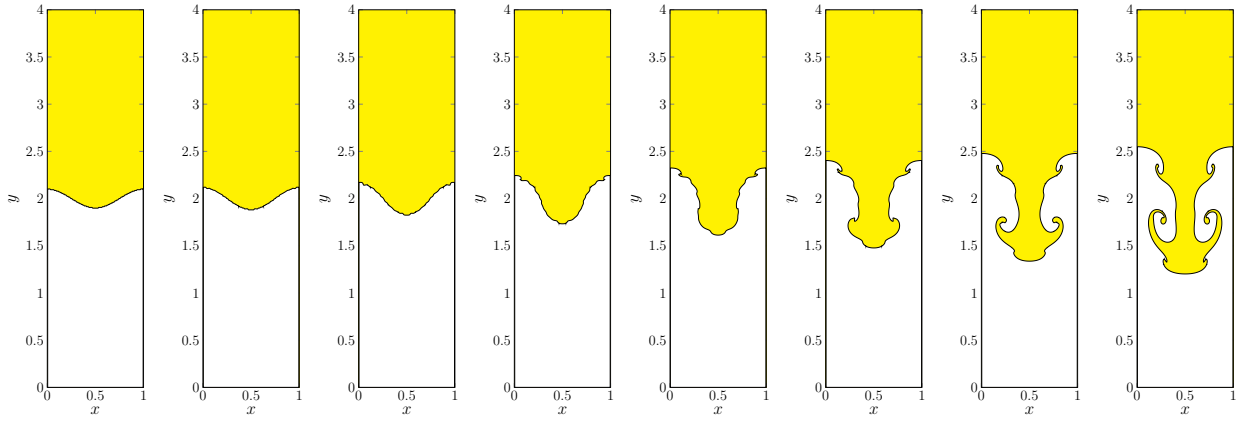

(b) Rayleigh-Taylor test results using our method.

Fig. 19: Rayleigh-Taylor test at times $t = 0, 1, 1.25, 1.5, 1.75, 2, 2.25, 2.5$ and density ratio of 3.

The initial placement of the drop gives an interface contact angle $\theta = 90°$. By varying the angle set in the bottom boundary condition $\mathbf{n} \cdot \nabla\hat{\gamma}^{n+1}$, we can cause a mismatch between the drop placement and the boundary condition contact angle. This mismatch will cause the drop to change shape as the phase-field evolves so that the interface

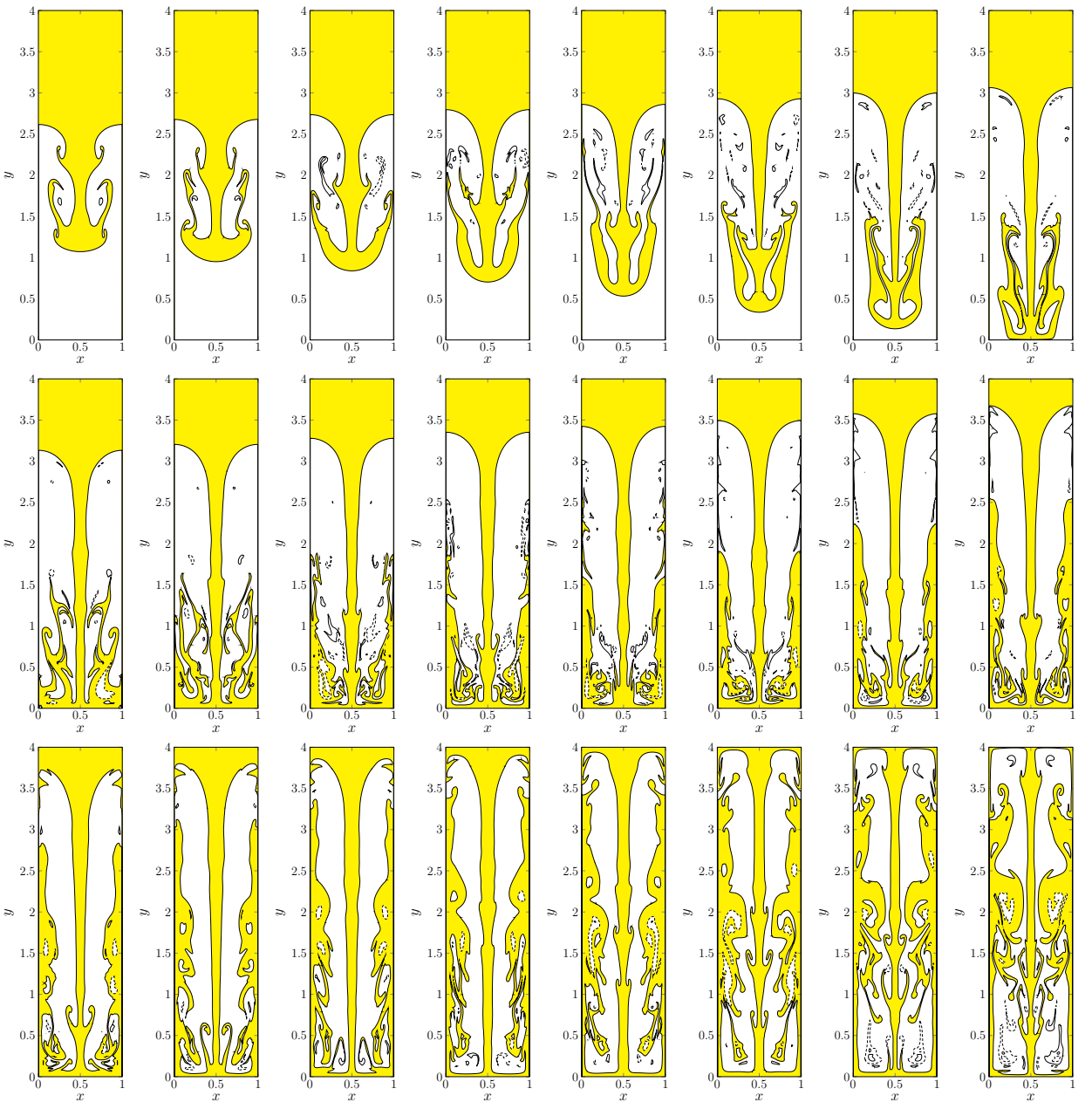

Fig. 20: Rayleigh-Taylor test results with $\rho_0 = 3$, from $t = 2.25$ to $t = 8$ in 0.25 increments.

contact angle will match the boundary condition. In Figure 26 we demonstrate the enforcement of boundary contact angles on the bottom boundary with $\theta = 90°, 45°, 135°, 60°, 120°$. Visually, our results are comparable to those presented in [31].

6. Conclusion

In this paper we constructed a novel, simple, and highly stable discretization of the Cahn-Hilliard equation. We coupled this to the Navier-Stokes equations to simulate phase separation in a two-phase fluid flow in two dimensions. We demonstrate that the resulting scheme is second order accurate in γ and velocity and compare it with published results on a number of tests. The scheme is mass-momentum consistent and works with large density ratios.

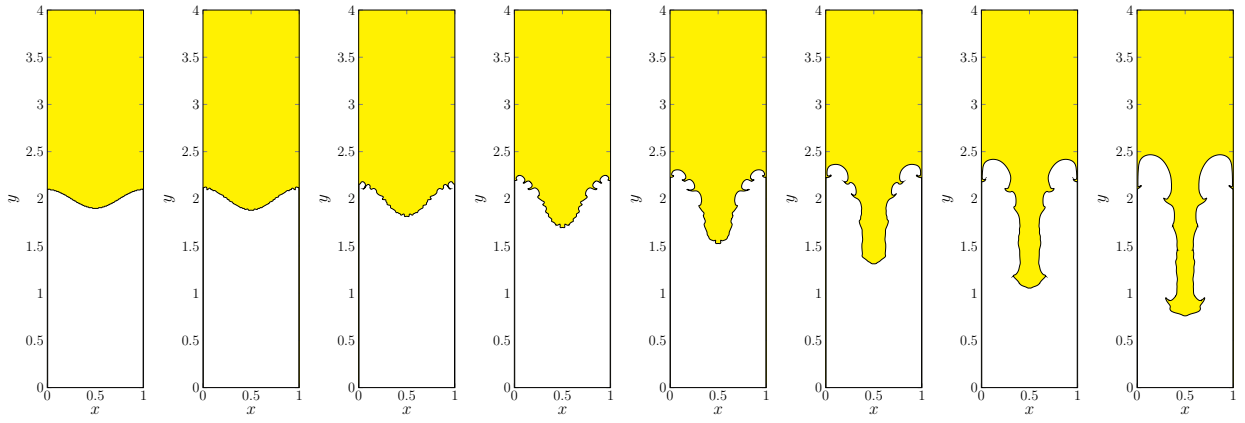

(a) $\rho_1 = 30$

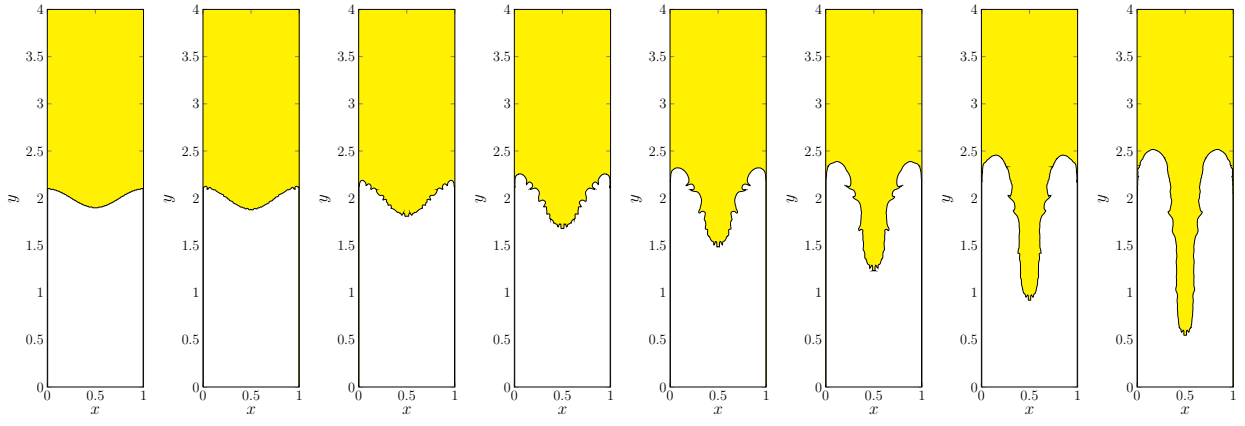

(b) $\rho_1 = 1000$

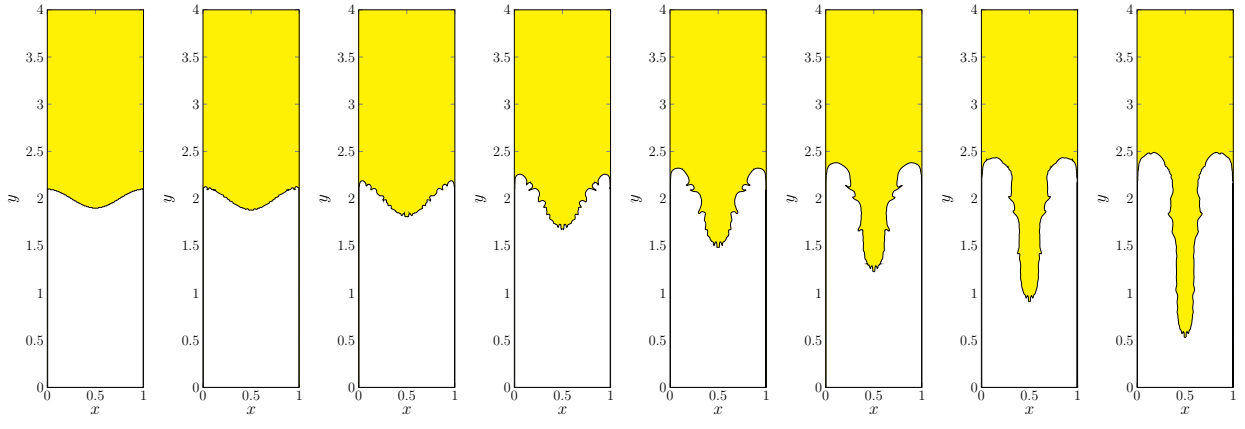

(c) $\rho_1 = 3000$

Fig. 21: Rayleigh-Taylor simulation with density ratio of 30, 1000 and 3000 at times $t = 0, 0.25, 0.5, 0.75, 1, 1.25, 1.5, 1.75$.

We also replace existing discretizations of the surface tension force on phase-field variables with one that has finite support around the transition region. The model has a parameter that allows it to transition from a smoothed continuum surface force to a fully sharp interface formulation, in which case the surface tension applied is equivalent to a sharp interface treatment using jump conditions. We compared our formulation of surface tension against other surface treatments used for the Cahn-Hilliard Navier-Stokes equations and found that our treatment compares favorably.

We have also noticed some limitations in the proposed scheme. As noted in Section 5.5, shearing flows with sharp γ transitions can lead to artifacts, though these are observed to diminish with refinement. The consistent advection

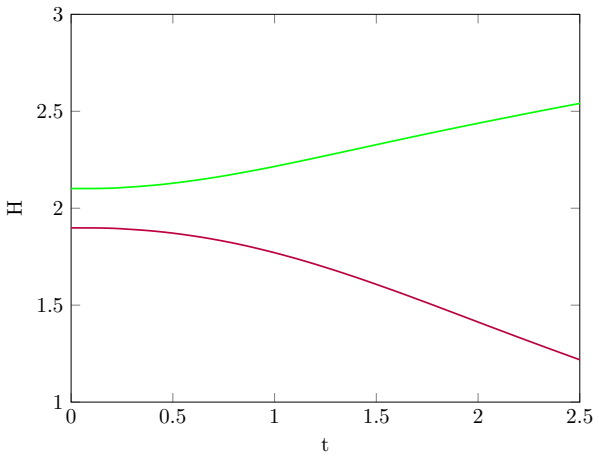

Fig. 22: Location of the maximum and minimum x of the interface in the Rayleigh-Taylor test with density ratio of 3.

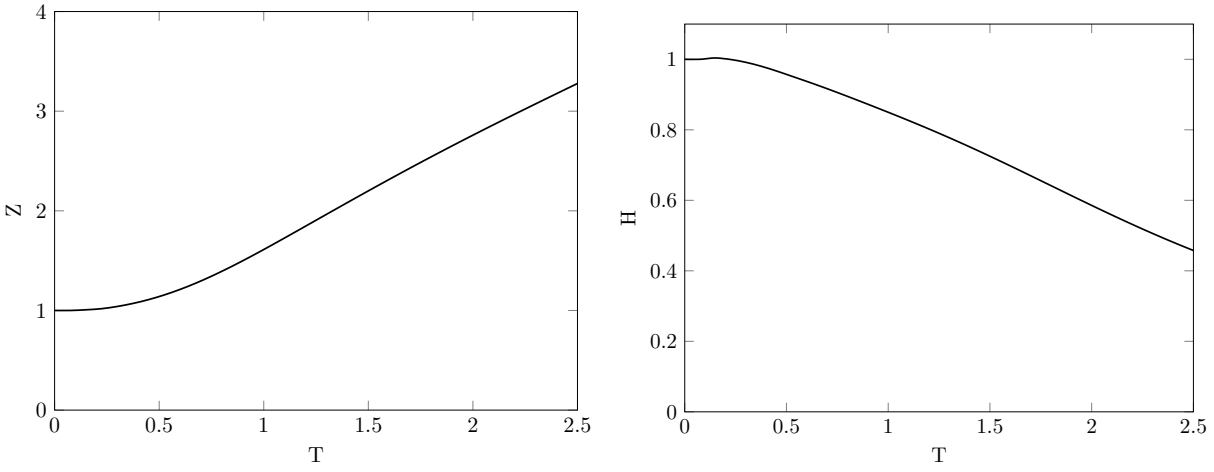

(a) Location of the front of fluid phase 1.

(b) Location of the height of fluid phase 1.

Fig. 23: Fluid height and front over time in the dam break test.

used for the momentum equations are generally observed to be less numerically robust than a more classical WENO-based advection scheme. We have also observed that the evolution of γ can produce values outside the range $[0, 1]$, which can lead to negative densities if the density ratio is large. We correct this using the gamma redistribution scheme from [30], though we note that this redistribution is effectively global and thus less than ideal. In our implementation, it also comes at the cost of an additional Poisson solve; a more physically plausible solution to this problem is desirable.

7. Acknowledgements

This work was supported in part by National Science Foundation award NSF-2006570 as well as University of California award M23PL6076.

References

[1] Rüyam Acar. Simulation of interface dynamics: a diffuse-interface model. *The Visual Computer*, 25(2):101–115, 2009.

[2] VE Badalassi and S Banerjee. Nano-structure computation with coupled momentum phase ordering kinetics models. *Nuclear engineering and design*, 235(10-12):1107–1115, 2005.

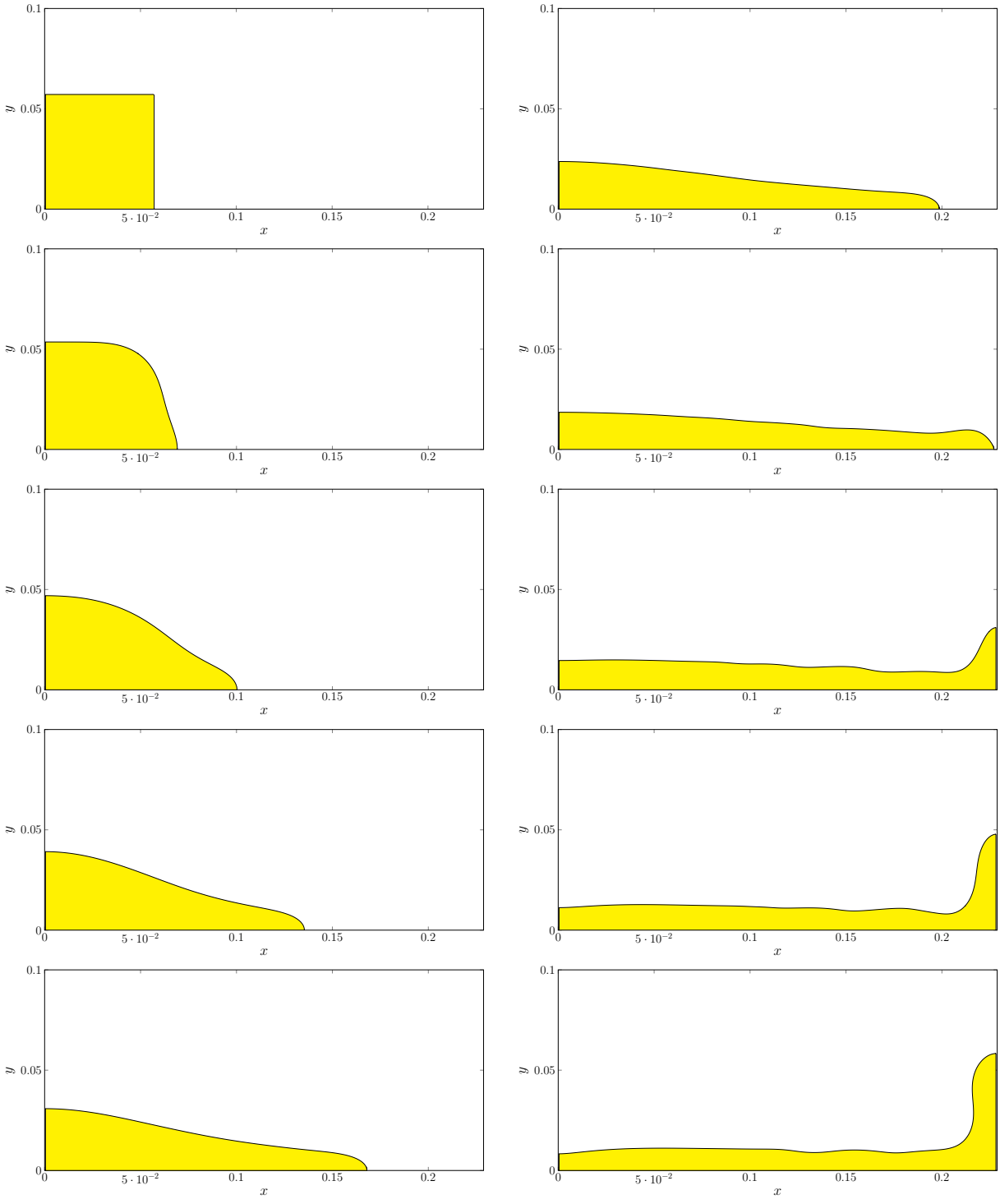

(a) $T = 0$ to $T = 2$

(b) $t = 2.5$ to $t = 5$

Fig. 24: The evolution of the dam break test with water and air from $T = 0$ to $T = 5$ in 0.5 increments.

[3] Vittorio E Badalassi, Hector D Ceniceros, and Sanjoy Banerjee. Computation of multiphase systems with phase field models. *Journal of computational physics*, 190(2):371–397, 2003.

[4] John W Barrett, James F Blowey, and Harald Garcke. Finite element approximation of the cahn–hilliard equation with degenerate mobility. *SIAM Journal on Numerical Analysis*, 37(1):286–318, 1999.

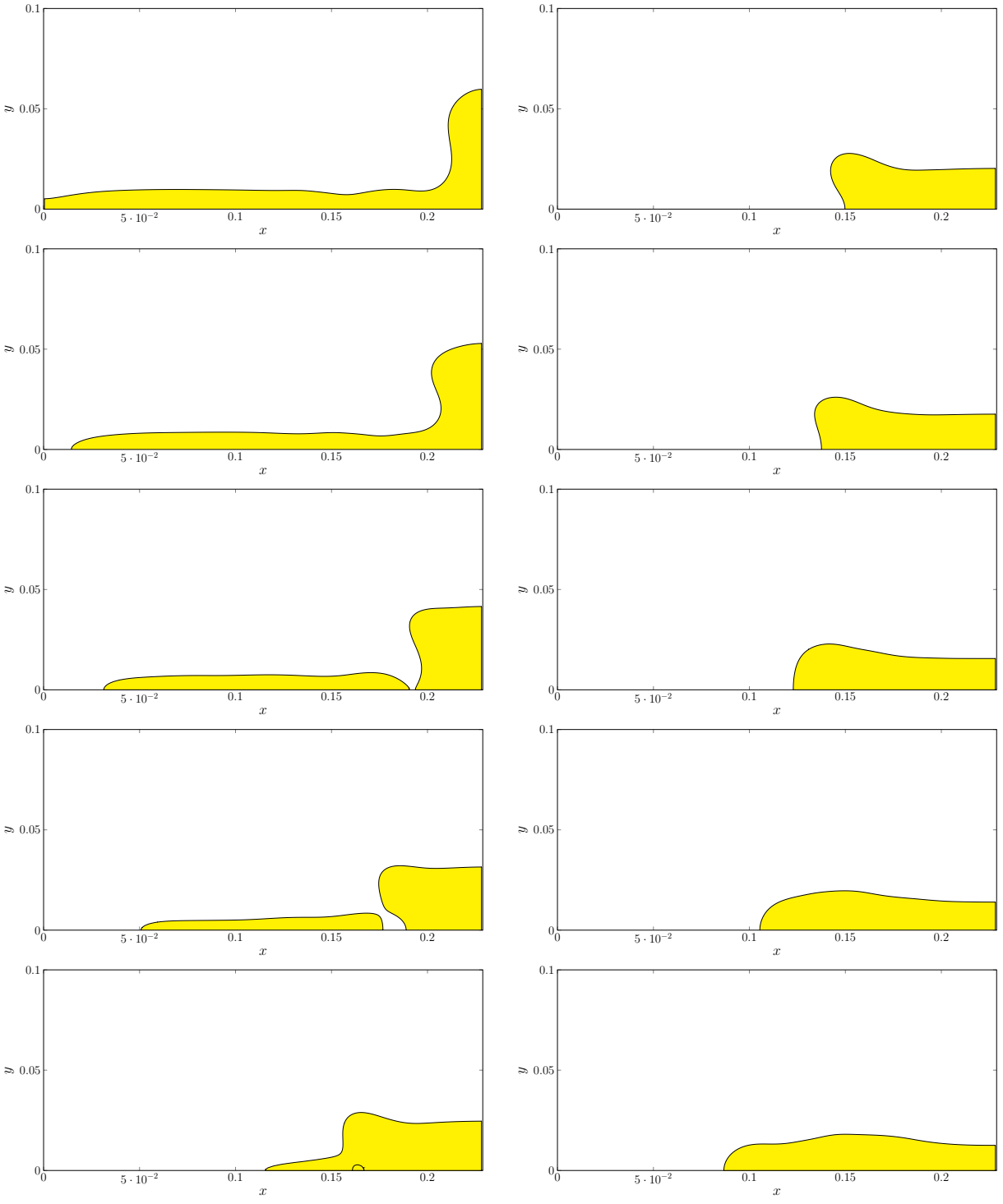

(a) $T = 5$ to $T = 7$

(b) $T = 7.5$ to $T = 9.5$

Fig. 25: The evolution of the dam break test with water and air from $T = 5$ to $T = 9.5$ in 0.5 increments.

[5] James F Blowey, MIM Copetti, and Charles M Elliott. Numerical analysis of a model for phase separation of a multicomponent alloy. *IMA Journal of Numerical Analysis*, 16(1):111–139, 1996.

[6] Jeremiah U Brackbill, Douglas B Kothe, and Charles Zemach. A continuum method for modeling surface tension. *Journal of computational physics*, 100(2):335–354, 1992.

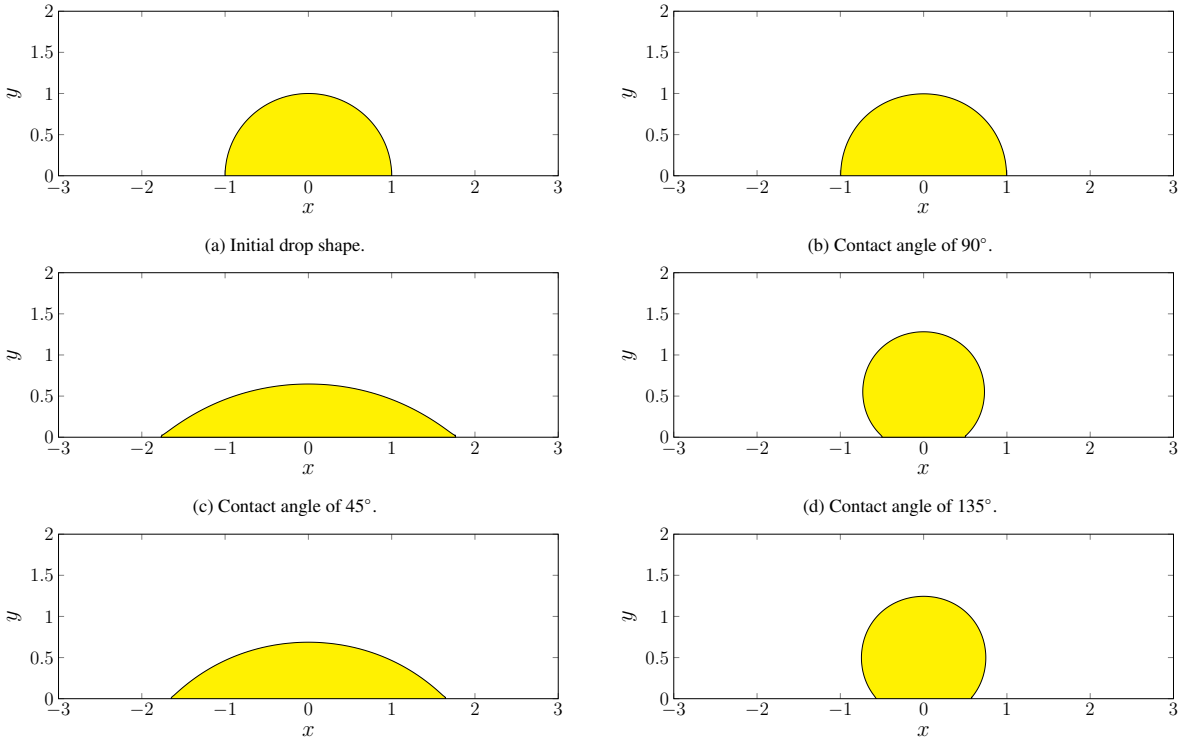

(a) Initial drop shape.

(b) Contact angle of 90°.

(c) Contact angle of 45°.

(d) Contact angle of 135°.

(e) Contact angle of 60°.

(f) Contact angle of 120°.

Fig. 26: Demonstration of the effects of the contact angle θ on a drop at rest.

[7] Markus Bussmann, Douglas B Kothe, and James M Sicilian. Modeling high density ratio incompressible interfacial flows. In *Fluids Engineering Division Summer Meeting*, volume 36150, pages 707–713, 2002.

[8] John W. Cahn and John E. Hilliard. Free energy of a nonuniform system. i. interfacial free energy. *The Journal of Chemical Physics*, 28(2): 258–267, 1958. doi: 10.1063/1.1744102. URL `https://doi.org/10.1063/1.1744102`.

[9] Kelong Cheng, Wenqiang Feng, Cheng Wang, and Steven M Wise. An energy stable fourth order finite difference scheme for the cahn–hilliard equation. *Journal of Computational and Applied Mathematics*, 362:574–595, 2019.

[10] Alexandre Joel Chorin. Numerical solution of the navier-stokes equations. *Mathematics of computation*, 22(104):745–762, 1968.

[11] Bart J. Daly. Numerical Study of Two Fluid Rayleigh-Taylor Instability. *The Physics of Fluids*, 10(2):297–307, 02 1967. ISSN 0031-9171. doi: 10.1063/1.1762109. URL `https://doi.org/10.1063/1.1762109`.

[12] Hang Ding, Peter D.M. Spelt, and Chang Shu. Diffuse interface model for incompressible two-phase flows with large density ratios. *Journal of Computational Physics*, 226(2):2078–2095, 2007. ISSN 0021-9991. doi: https://doi.org/10.1016/j.jcp.2007.06.028. URL `https://www.sciencedirect.com/science/article/pii/S0021999107002793`.

[13] S. Dong. On imposing dynamic contact-angle boundary conditions for wall-bounded liquid–gas flows. *Computer Methods in Applied Mechanics and Engineering*, 247-248:179–200, 2012. ISSN 0045-7825. doi: https://doi.org/10.1016/j.cma.2012.07.023. URL `https://www.sciencedirect.com/science/article/pii/S004578251200254X`.

[14] Suchuan Dong and Jie Shen. A time-stepping scheme involving constant coefficient matrices for phase-field simulations of two-phase incompressible flows with large density ratios. *Journal of Computational Physics*, 231(17):5788–5804, 2012.

[15] Charles M Elliott. The cahn-hilliard model for the kinetics of phase separation. In *Mathematical models for phase change problems*, pages 35–73. Springer, 1989.

[16] Charles M Elliott and Donald A French. A nonconforming finite-element method for the two-dimensional cahn–hilliard equation. *SIAM Journal on Numerical Analysis*, 26(4):884–903, 1989.

[17] Xiaobing Feng and Andreas Prohl. Error analysis of a mixed finite element method for the cahn-hilliard equation. *Numerische Mathematik*, 99:47–84, 2004.

[18] Marianne M. Francois, Sharen J. Cummins, Edward D. Dendy, Douglas B. Kothe, James M. Sicilian, and Matthew W. Williams. A balanced-force algorithm for continuous and sharp interfacial surface tension models within a volume tracking framework. *Journal of Computational Physics*, 213(1):141–173, March 2006. ISSN 00219991. doi: 10.1016/j.jcp.2005.08.004. URL `https://linkinghub.elsevier.com/retrieve/pii/S0021999105003748`.

[19] Daisuke Furihata. A stable and conservative finite difference scheme for the cahn-hilliard equation. *Numerische Mathematik*, 87(4):675–699, 2001.

[20] J.-L. Guermond and L. Quartapelle. A projection fem for variable density incompressible flows. *Journal of Computational Physics*, 165(1):167–188, 2000. ISSN 0021-9991. doi: https://doi.org/10.1006/jcph.2000.6609. URL `https://www.sciencedirect.com/science/article/pii/S0021999100966099`.

[21] Francisco Guillén-González and Giordano Tierra. On linear schemes for a cahn–hilliard diffuse interface model. *Journal of Computational Physics*, 234:140–171, 2013.

[22] Francisco Guillén-González and Giordano Tierra. Second order schemes and time-step adaptivity for allen–cahn and cahn–hilliard models. *Computers & Mathematics with Applications*, 68(8):821–846, 2014.

[23] Zhenlin Guo, Ping Lin, J Lowengrub, and Steven M Wise. Mass conservative and energy stable finite difference methods for the quasi-incompressible navier–stokes–cahn–hilliard system: Primitive variable and projection-type schemes. *Computer Methods in Applied Mechanics and Engineering*, 326:144–174, 2017.

[24] Morton E Gurtin, Debra Polignone, and Jorge Vinals. Two-phase binary fluids and immiscible fluids described by an order parameter. *Mathematical Models and Methods in Applied Sciences*, 6(06):815–831, 1996.

[25] F. Harlow and E. Welch. Numerical calculation of time dependent viscous flow of fluid with a free surface. *Phys Fluid*, 8(12):2182–2189, 1965.

[26] Qiaolin He, Roland Glowinski, and Xiao-Ping Wang. A least-squares/finite element method for the numerical solution of the navier–stokes-cahn–hilliard system modeling the motion of the contact line. *Journal of computational physics*, 230(12):4991–5009, 2011.

[27] Qunwu He and Nobuhide Kasagi. Phase-field simulation of small capillary-number two-phase flow in a microtube. *Fluid dynamics research*, 40(7-8):497, 2008.

[28] Yinnian He, Yunxian Liu, and Tao Tang. On large time-stepping methods for the cahn–hilliard equation. *Applied Numerical Mathematics*, 57(5-7):616–628, 2007.

[29] Pierre C Hohenberg and Bertrand I Halperin. Theory of dynamic critical phenomena. *Reviews of Modern Physics*, 49(3):435, 1977.

[30] Ziyang Huang, Guang Lin, and Arezoo M Ardekani. Consistent and conservative scheme for incompressible two-phase flows using the conservative allen-cahn model. *Journal of Computational Physics*, 420:109718, 2020.

[31] Ziyang Huang, Guang Lin, and Arezoo M. Ardekani. Consistent, essentially conservative and balanced-force phase-field method to model incompressible two-phase flows. *Journal of Computational Physics*, 406:109192, 2020. ISSN 0021-9991. doi: https://doi.org/10.1016/j.jcp.2019.109192. URL `https://www.sciencedirect.com/science/article/pii/S0021999119308976`.

[32] David Jacqmin. Calculation of two-phase navier–stokes flows using phase-field modeling. *Journal of Computational Physics*, 155(1):96–127, 1999. ISSN 0021-9991. doi: https://doi.org/10.1006/jcph.1999.6332. URL `https://www.sciencedirect.com/science/article/pii/S0021999199963325`.

[33] Guang-Shan Jiang and Chi-Wang Shu. Efficient implementation of weighted eno schemes. *Journal of computational physics*, 126(1): 202–228, 1996.

[34] Myungjoo Kang, Ronald P Fedkiw, and Xu-Dong Liu. A boundary condition capturing method for multiphase incompressible flow. *Journal of scientific computing*, 15:323–360, 2000.

[35] Junseok Kim. A continuous surface tension force formulation for diffuse-interface models. *Journal of computational physics*, 204(2): 784–804, 2005.

[36] Junseok Kim. Phase field computations for ternary fluid flows. *Computer methods in applied mechanics and engineering*, 196(45-48): 4779–4788, 2007.

[37] Junseok Kim. A generalized continuous surface tension force formulation for phase-field models for multi-component immiscible fluid flows. *Computer Methods in Applied Mechanics and Engineering*, 198(37-40):3105–3112, 2009.

[38] Junseok Kim. Phase-field models for multi-component fluid flows. *Communications in Computational Physics*, 12(3):613–661, 2012.

[39] Junseok Kim and John Lowengrub. Phase field modeling and simulation of three-phase flows. *Interfaces and free boundaries*, 7(4):435–466, 2005.

[40] Benjamin Lalanne, Lucia Rueda Villegas, Sébastien Tanguy, and Frédéric Risso. On the computation of viscous terms for incompressible two-phase flows with level set/ghost fluid method. *Journal of Computational Physics*, 301:289–307, 2015.

[41] Dongsun Lee, Joo-Youl Huh, Darae Jeong, Jaemin Shin, Ana Yun, and Junseok Kim. Physical, mathematical, and numerical derivations of the cahn–hilliard equation. *Computational Materials Science*, 81:216–225, 2014.

[42] Yibao Li, Hyun Geun Lee, Binhu Xia, and Junseok Kim. A compact fourth-order finite difference scheme for the three-dimensional cahn–hilliard equation. *Computer Physics Communications*, 200:108–116, 2016.

[43] Yibao Li, Yongho Choi, and Junseok Kim. Computationally efficient adaptive time step method for the cahn–hilliard equation. *Computers & Mathematics with Applications*, 73(8):1855–1864, 2017.

[44] Chun Liu and Jie Shen. A phase field model for the mixture of two incompressible fluids and its approximation by a fourier-spectral method. *Physica D: Nonlinear Phenomena*, 179(3-4):211–228, 2003.

[45] Haihu Liu and Yonghao Zhang. Phase-field modeling droplet dynamics with soluble surfactants. *Journal of Computational Physics*, 229(24): 9166–9187, 2010.

[46] JC Martin and WJ Moyce. An experimental study of the collapse of fluid columns on a rigid horizontal plane, in a medium of lower, but comparable, density. 5. *Philosophical Transactions of the Royal Society of London Series A-Mathematical and Physical Sciences*, 244(882): 325–334, 1952.

[47] Mark Owkes and Olivier Desjardins. A mass and momentum conserving unsplit semi-lagrangian framework for simulating multiphase flows. *Journal of Computational Physics*, 332:21–46, 2017.

[48] Mehdi Raessi and Heinz Pitsch. Consistent mass and momentum transport for simulating incompressible interfacial flows with large density ratios using the level set method. *Computers & Fluids*, 63:70–81, 2012.

[49] Rayleigh. Investigation of the Character of the Equilibrium of an Incompressible Heavy Fluid of Variable Density*. *Proceedings of the London Mathematical Society*, s1-14(1):170–177, 11 1882. ISSN 0024-6115. doi: 10.1112/plms/s1-14.1.170. URL `https://doi.org/10.1112/plms/s1-14.1.170`.

[50] Somnath Santra, Shubhadeep Mandal, and Suman Chakraborty. Phase-field modeling of multicomponent and multiphase flows in microfluidic systems: A review. *International Journal of Numerical Methods for Heat & Fluid Flow*, 31(10):3089–3131, 2020.

[51] Jie Shen and Xiaofeng Yang. Energy stable schemes for cahn-hilliard phase-field model of two-phase incompressible flows. *Chinese Annals of Mathematics, Series B*, 31(5):743–758, 2010.

[52] Jie Shen and Xiaofeng Yang. A phase-field model and its numerical approximation for two-phase incompressible flows with different densities and viscosities. *SIAM Journal on Scientific Computing*, 32(3):1159–1179, 2010.

[53] Jie Shen and Xiaofeng Yang. Decoupled, energy stable schemes for phase-field models of two-phase incompressible flows. *SIAM Journal on Numerical Analysis*, 53(1):279–296, 2015.

[54] Knut Erik Teigen, Peng Song, John Lowengrub, and Axel Voigt. A diffuse-interface method for two-phase flows with soluble surfactants. *Journal of computational physics*, 230(2):375–393, 2011.

[55] Grétar Tryggvason. Numerical simulations of the rayleigh-taylor instability. *Journal of Computational Physics*, 75(2):253–282, 1988. ISSN 0021-9991. doi: https://doi.org/10.1016/0021-9991(88)90112-X. URL `https://www.sciencedirect.com/science/article/pii/002199918890112X`.

[56] Bao-Shan Wang, Peng Li, Zhen Gao, and Wai Sun Don. An improved fifth order alternative weno-z finite difference scheme for hyperbolic conservation laws. *Journal of Computational Physics*, 374:469–477, 2018.

[57] Garth N Wells, Ellen Kuhl, and Krishna Garikipati. A discontinuous galerkin method for the cahn–hilliard equation. *Journal of Computational Physics*, 218(2):860–877, 2006.

[58] Steven M Wise, John S Lowengrub, Hermann B Frieboes, and Vittorio Cristini. Three-dimensional multispecies nonlinear tumor growth—i: model and numerical method. *Journal of theoretical biology*, 253(3):524–543, 2008.

[59] Qing Xia, Junxiang Yang, and Yibao Li. On the conservative phase-field method with the n-component incompressible flows. *Physics of Fluids*, 35(1), 2023.

[60] Xiaofeng Yang, James J Feng, Chun Liu, and Jie Shen. Numerical simulations of jet pinching-off and drop formation using an energetic variational phase-field method. *Journal of Computational Physics*, 218(1):417–428, 2006.

[61] Pengtao Yue, James J Feng, Chun Liu, and Jie Shen. A diffuse-interface method for simulating two-phase flows of complex fluids. *Journal of Fluid Mechanics*, 515:293–317, 2004.

[62] Pengtao Yue, James J Feng, Chun Liu, and Jie Shen. Diffuse-interface simulations of drop coalescence and retraction in viscoelastic fluids. *Journal of Non-Newtonian Fluid Mechanics*, 129(3):163–176, 2005.

[63] Guangpu Zhu, Jisheng Kou, Shuyu Sun, Jun Yao, and Aifen Li. Numerical approximation of a phase-field surfactant model with fluid flow. *Journal of Scientific Computing*, 80:223–247, 2019.

[64] Jingzhi Zhu, Long-Qing Chen, Jie Shen, and Veena Tikare. Coarsening kinetics from a variable-mobility cahn-hilliard equation: Application of a semi-implicit fourier spectral method. *Physical Review E*, 60(4):3564, 1999.